Transition of properties from a proton beam to a neutron beam using the ^{7}Li(p, n)^{7}Be reaction as an example

Stefan Schmidt

Contents

1. Introduction **1**

1.1. The *Fra*nkfurt *N*eutron Source at Stern-Gerlach-*Z*entrum (FRANZ) . 4

1.1.1. Time of flight mode 4

1.1.2. Activation mode 7

1.2. Neutron production reactions 8

1.3. The ^{7}Li(p, n)^{7}Be reaction 10

1.3.1. Compound nucleus reaction 10

1.3.2. Threshold 11

1.3.3. Kinematic collimation 12

1.3.4. Particle stopping 13

2. Implementation **15**

2.1. Requirements 15

2.2. Proton representation 15

2.3. Space charge 16

2.4. Time steps and target thickness 18

2.5. Interaction probability and scattering direction 20

2.6. Kinetic energy and transformation 22

2.7. Target description 23

2.8. Particle stopping 24

2.9. Technical information 25

3. Experiments **27**

3.1. Expectations 27

3.2. Measurements at Forschungszentrum Karlsruhe 29

3.3. Measurements at Physikalisch-Technische Bundesanstalt 34

4. Neutron beam properties at FRANZ **37**

5. Conclusion **47**

Bibliography **49**

A. Energy interchange **55**
A.1. Classical description 55
A.2. Relativistic description 58

B. Stopping power **63**

1. Introduction

Since their discovery in the 1930s, neutron applications have become vital to our modern world. Without nuclear fission reactors providing power in the gigawatts region technological as well as scientifical progress would be unthinkable. Although the first reactor was constructed in 1942 [1], the physics of neutrons is still an intricate topic of research. Nowadays, there are many neutron facilities around the world, each one built with a different set of parameters to focus on a specific aspect of the topic.

When the Forschungszentrum Karlsruhe intensified its research program in the 1980s with the development of a barium-fluoride detector [2], it concentrated on measurements of neutron capture cross sections in the keV region. If measured precisely, these data are valuable to a multitude of research fields ranging from nuclear waste disposal to knowledge about the age of the universe and heavy element synthesis.

The current way to determine the age of the universe is based on the observation of its expansion. Hubble realized [3] that the radial velocity v_r is a function of the distance to the observer d resulting in $v_r = H_0 \times d$. Since speed and distance are experimentally accessible, the Hubble parameter H_0 can be deduced from measurements. Assuming $H_0 = \text{const.}$, its reciprocal denotes the "Hubble time", the point in time at which the expansion started. Current measurements [4, 5] are in good agreement with $H_0 = 72\,\frac{\text{km}}{\text{s}\,\text{Mpc}}$ resulting in $t = \frac{1}{H_0} = 13.6$ billion years. However, these measurements are still affected by significant uncertainties. The investigation of the nucleosynthesis of the elements offers the possibility of an independent approach. If the decay times of the involved isotopes are similar to the age of the universe, their current abundances depend on their production rate. It results from the respective cross section and the production time, the latter of which gives a lower limit for the age of the universe.

In order to validate the results, a different approach may use data obtained from neutron cross section experiments. Differing sets of initial isotopic abundances should yield different abundances of heavy nuclei depending on the assumed age. By varying the initial conditions, a simulation should be able to predict the resulting abundances – if these match the abundances observed nowadays, this approach will offer an alternative estimation for the age of the universe.

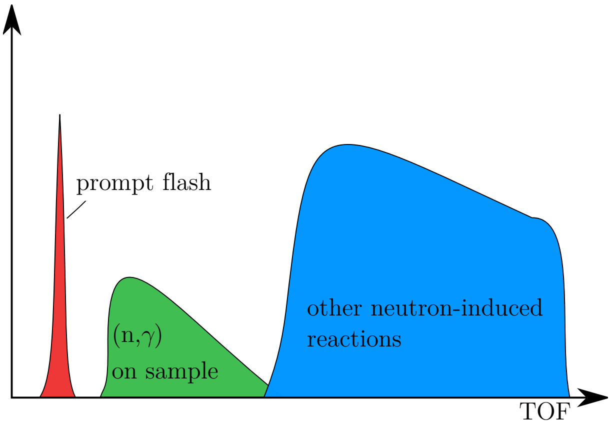

Figure 1.1.: Sample spectrum expected at FRANZ (adopted from [9, p. 218]). *Not to scale.*

Such an approach requires an understanding of the production of heavy nuclei. Before reaching their White Dwarf state, sun-like stars pass a Red Giant state where α reactions create nuclei that provide free neutrons for heavy element nucleosynthesis (cf. [6, p. 179]). Iron and similar nuclei capture these uncharged particles on a timescale of months or years while the β decay time of the created nuclei is typically much shorter. However, this process, called slow neutron capture process or s process, cannot explain certain neutron-rich nuclei like uranium (cf. [7, p. 200]). For these, even higher neutron fluxes are required – in supernovae fluxes are assumed to be about $4 \times 10^{32}\,\frac{1}{\mathrm{cm}^2\,\mathrm{s}}$ [8, p. 587].

In contrast, the FRANZ facility under construction at the Goethe University Frankfurt, which aims at very high fluxes, will only be able to provide neutron fluxes up to $10^{12}\,\frac{1}{\mathrm{cm}^2\,\mathrm{s}}$ in the energy region of 1–200 keV. To achieve this goal, a high-intensity proton beam is required that impinges on a conversion target. It consists of a $\approx 10\,\mu\mathrm{m}$ thick lithium layer evaporated onto a copper backing. Preferably, the layer will be made of metallic lithium as this can provide higher neutron intensities than a lithium compound. Either way, neutrons are produced via the ^{7}Li(p, n)^{7}Be reaction: ^{7}Li absorbs protons and the resulting nucleus de-excites by emitting neutrons. The neutral particles can then be used for subsequent measurements, e.g. neutron capture cross sections.

For these measurements, the FRANZ setup provides two different modes of operation. In time of flight operation, neutron fluxes of up to $10^7\,\frac{1}{\mathrm{cm}^2\,\mathrm{s}}$ can be achieved. After their production, which coincides with a gamma flash that is used to start the time of flight measurement (cf. Figure 1.1), the neutrons drift through a guiding tube until they react in (n, γ) reactions inside the sample. The gammas are detected in a 4π BaF_2 detector array (cf. Figure 1.2) that covers the full solid angle with

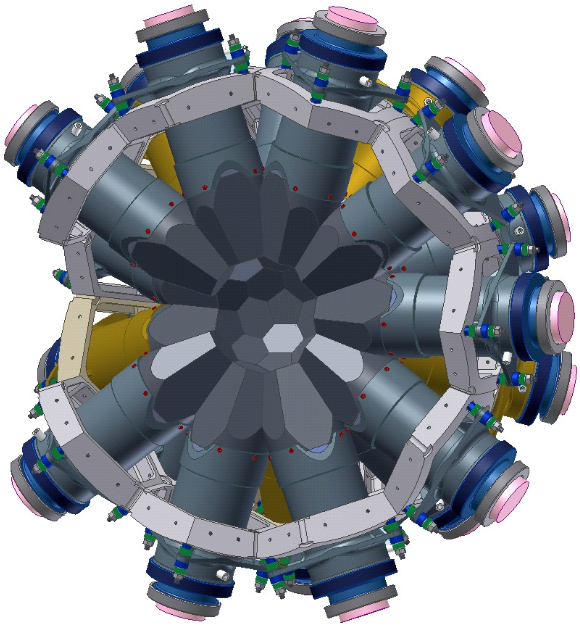

Figure 1.2.: Cut-open view of the BaF_2 detector array used for the measurement of neutron capture cross-sections.

42 detector modules mounted in a honeycomb frame. Each module consists of a photomultiplier driven by a voltage divider, and a BaF_2 crystal. Inside the crystal, gammas cause scintillation light that the photomultiplier converts to an electrical signal and then amplifies. The sum energy from all photons is the most important signature of a capture event. The energy resolution of BaF_2 enables this material to distinguish such events from others and provides sub-nanosecond time resolution [10] which is important for neutron energy determination using the time of flight method.

In activation mode, the setup is able to achieve a neutron flux of $10^{12}\,\frac{1}{\mathrm{cm}^2\,\mathrm{s}}$ at the sample. It is affixed closely to the neutron production target and sandwiched by gold foils. The cross section is then measured relative to the well-known cross section of gold. The properties of the neutron beam are mostly determined by the incident proton beam and the target thickness. While there are several codes available that aim at describing the ^{7}Li(p, n) and possibly other reactions, none was found to allow the analysis of per-particle data, which is required to study the transformation of beam properties. To alleviate the situation, in the context of this work a computer code has been developed that can simulate the ^{7}Li(p, n)^{7}Be reaction while retaining a high degree of information both in the input and in the output channel.

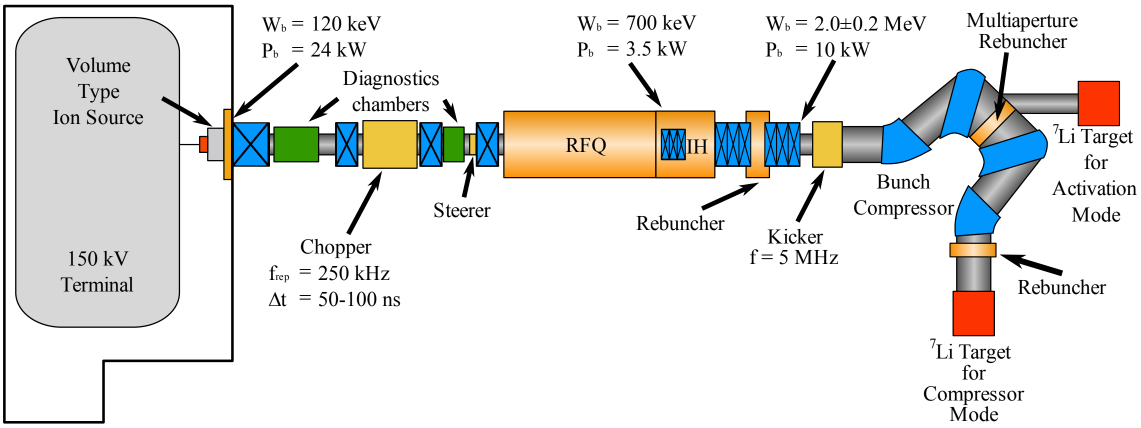

Figure 1.3.: Overview of the FRANZ neutron source currently under construction at the Goethe University Frankfurt.
Not to scale.

1.1. The *Fra*nkfurt *N*eutron Source at Stern-Gerlach-*Z*entrum (FRANZ)

In the FRANZ facility (cf. Figure 1.3), a volume type ion source will provide a proton beam of $I = 200\,\mathrm{mA}$ with a proton fraction of approximately $90\,\%$ [11, 12]. It features a pentode extraction system [13] which decouples the extraction from the initial acceleration. In this design, the first two electrodes are used to optimize the plasma meniscus, while the remaining three electrodes solely handle acceleration of the extracted ions. The latter set is comprised of two ground electrodes with a central third electrode that is set to negative potential. It screens the plasma chamber from electrons that otherwise would enter the source. Without this screening electrode, the charge distribution within the plasma may change, complicating the controlled extraction of a certain type of ion. More importantly, the beam's space charge is not compensated at the ion source exit leading to a significant increase in divergence angles [14, p. 63]. Behind the source, the emitted particles enter the low energy beam transport (LEBT) section. Depending on the operation mode of the accelerator based neutron source, the use of subsequent components differs.

1.1.1. Time of flight mode

In time of flight operation, a chopper system [15, 16] in the LEBT section fragments the beam into pulses of $t_{\mathrm{pulse}} \approx 50\text{–}100\,\mathrm{ns}$ length. It operates at a repetition

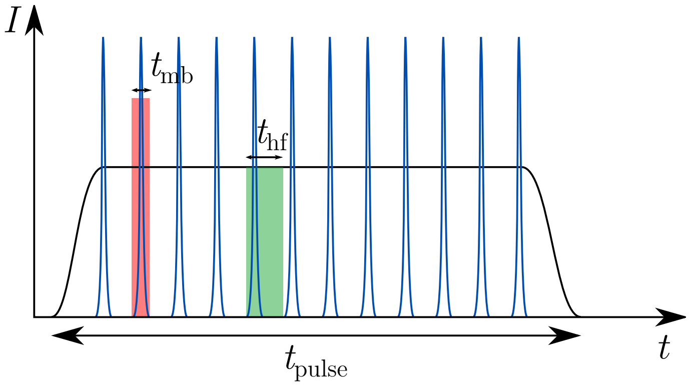

Figure 1.4.: After the chopper, the direct current beam is split up into short pulses of $t_{\mathrm{pulse}} \approx 50$–$100\,\mathrm{ns}$ length (black). In the linear acceleration section, these pulses are compressed into micro bunches of $t_{\mathrm{mb}} = 1\,\mathrm{ns}$ length (blue). The average charge Q_{mb} of a single micro bunch is denoted by semi-transparent boxes, both of which have the same area indicating that $Q_{\mathrm{mb}} = \mathrm{const.}$
Not to scale.

frequency of 250 kHz resulting in a duty cycle of

$$D = 50\,\mathrm{ns} \times 250\,\mathrm{kHz} \approx 1\,\% \tag{1.1}$$

Therefore, the average beam current drops to one hundredth of the initial value while the peak current during t_{pulse} stays at 200 mA. The remaining fraction, i.e. $1 - D \approx 99\,\%$, has to be dumped safely. Thus, sweep times from the beam axis to the dump have to be very low in order to reduce stress on the beam tube walls.

After the chopper, the beam pulses continue towards the linear acceleration section. There, a radio-frequency quadrupole (RFQ) and an interdigital H mode (IH) structure increase the beam energy to its design value of $E_{\mathrm{p}} = 2\,\mathrm{MeV}$. Both components operate at 175 MHz, so the high-frequency period with a mean current of $I_{\mathrm{hf,avg}} = 150\,\mathrm{mA}$ is $t_{\mathrm{hf}} = 1/175\,\mathrm{MHz} \approx 5.7\,\mathrm{ns}$ long. A single bunch is shorter than that by a factor of six because of phase width compression from 360° to 60° (compression ratio $\eta_{\mathrm{hf}} = 6$). Ideally, in this section particles are neither produced nor lost, so the average micro bunch current increases by the compression factor to $I_{\mathrm{mb,avg}} = 6 \times 150\,\mathrm{mA} = 900\,\mathrm{mA}$ with even higher peak currents. The total charge of a bunch is given by

$$\begin{aligned} Q_{\mathrm{mb}} &= I_{\mathrm{mb,avg}}\, t_{\mathrm{mb}} \\ &= I_{\mathrm{hf,avg}}\, t_{\mathrm{hf}} \\ &= \frac{150\,\mathrm{mA}}{175\,\mathrm{MHz}} \\ &= 8.5714 \times 10^{-10}\,\mathrm{C} \end{aligned}$$

In order to enhance the proton flux on the target a Mobley type bunch compressor [17] merges up to nine successive micro bunches into a single pulse of $t_{\mathrm{pulse,target}} = t_{\mathrm{mb}} = 1\,\mathrm{ns}$ length bringing the total compression ratio of FRANZ to $\eta_{\mathrm{total}} = 9 \times 6 = 54$. The construction of the compressor is very ambitious due to the precision required for path lengths and magnet design. Strong space charge forces within each micro bunch require duplex-gradient dipoles [18] for advanced edge focussing as well as a rebuncher cavity within the compressor. After compressing the micro bunches, the device delivers a total charge of

$$\begin{aligned} Q_{\mathrm{at\ target}} &\approx 9\, Q_{\mathrm{mb}} \\ &= 7.7143 \times 10^{-9}\,\mathrm{C} \end{aligned} \tag{1.2}$$

equivalent to a proton count of

$$N_{\mathrm{p}} = \frac{Q_{\mathrm{at\ target}}}{e} = 4.815 \times 10^{10} \tag{1.3}$$

Assuming a cylindrical shape for the bunch, current estimations with bunch radius $r \approx 0.62\,\mathrm{cm}$ and length $l = 1.57\,\mathrm{cm}$ yield a proton density on the order of $10^{10}\,\mathrm{cm}^{-3}$.

The compressed proton pulse continues to the last rebuncher, which can also vary the proton energy by ±200 keV, and finally hits the neutron production target. The target's most important constituent, lithium, is either used in its metallic form or in a thermally more stable compound, which reduces the expected neutron flux significantly. The layer relevant to neutron production is $\approx 10\,\mu\mathrm{m}$ thick and evaporated on a water-cooled copper backing that removes the heat of the $P_{\mathrm{avg}} = 4\,\mathrm{kW}$ beam [19]. In this layer, the protons from a FRANZ pulse with $E_{\mathrm{p}} = 2\,\mathrm{MeV}$ release

$$E_{\mathrm{depos,target}} \approx 6 \times 10^{-4}\,\mathrm{J}$$

which results in a peak power deposition of ($t_{\mathrm{pulse,target}} = 1\,\mathrm{ns}$, see above)

$$\begin{aligned} P_{\mathrm{peak}} &= \frac{E_{\mathrm{depos,target}}}{t_{\mathrm{pulse,target}}} \\ &\approx 6 \times 10^{5}\,\mathrm{W} \end{aligned}$$

Considering that the volume in which P_{peak} deposited is determined by the beam radius of $r \approx 0.6\,\mathrm{cm}$ and a lithium layer thickness of $d = 10\,\mu\mathrm{m}$ [19], the peak power density yields

$$\frac{P_{\mathrm{peak}}}{\pi\, r^2\, d} \approx 5 \times 10^8\, \frac{\mathrm{W}}{\mathrm{cm}^3}$$

When hitting the ^{7}Li target, gammas and neutrons are produced. The neutrons are collimated on their way to the sample, which is positioned in the center of a 4π $\mathrm{BaF_2}$ detector array. The array is comprised of 42 detector modules that can detect gammas from neutron capture reaction across the full solid angle. The collimation tube from the production target to the sample shields the detector from neutrons that would otherwise hit one of the detector modules causing an unwanted background. When the neutrons react in the sample, the gammas produced cause scintillation light in the $\mathrm{BaF_2}$ crystals of the modules. It is converted to an electrical signal using a photomultiplier tube attached to the crystals. Since the initial gamma flash and (n, γ) events are recorded by the detector, the corresponding time difference can be used to determine the time of flight t_{tof}. Together with the known distance between target and sample of $d_{\mathrm{ts}} = 80\,\mathrm{cm}$, the neutron velocity v_{n} can be derived using

$$v_{\mathrm{n}} = \frac{d_{\mathrm{ts}}}{t_{\mathrm{tof}}}$$

The kinetic energy can then be calculated using

$$E_{\mathrm{n}} = \left(\frac{1}{\sqrt{1 - \frac{v_{\mathrm{n}}^2}{c^2}}} - 1 \right) m_{\mathrm{n}} c^2$$

or non-relativistically with

$$E_{\mathrm{n}} = \frac{1}{2}\, m_{\mathrm{n}}\, v_{\mathrm{n}}^2$$

Since expected neutron energies only range up to $E_{\mathrm{n,max}} \approx 500\,\mathrm{keV}$ [11] (corresponding to $v/c \approx 3\,\%$), non-relativistic formulas can be used.

Experimentally, this approach is very feasible although the energy measurement may suffer from uncertainties, for example from the time resolution due to the finite length of the proton pulses.

1.1.2. Activation mode

In activation mode, the chopper is not used, the proton beam passes through the component unmodified. As in time of flight mode, the following RFQ and IH cavity raise the beam energy to $E_{\mathrm{p}} = 2\,\mathrm{MeV} \pm 0.2\,\mathrm{MeV}$. There, the direct current (dc) beam from the source turns into a continuous wave (cw) beam because of the periodic

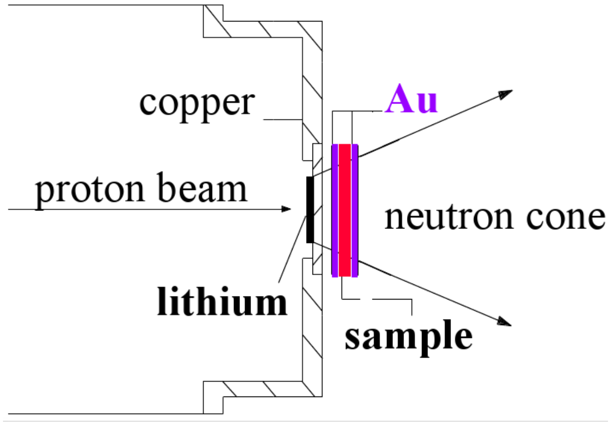

Figure 1.5.: Setup of the activation target (reproduced from [20]).
Not to scale.

operation of both devices. Next, the protons pass the unused bunch compressor finally hitting the activation target, which consists of the sample under investigation sandwiched between two gold foils (see Figure 1.5). They enable a measurement of the cross section relative to gold, for which energy-dependent data are well-known [2, p. 613]. After sufficient irradiation the three-layer sample is removed from the beam line and its decays are measured separately. Beside the determination of cross sections, this mode also enables tests of detectors for reliability and durability when exposed to high neutron fluxes.

1.2. Neutron production reactions

For accelerator-based neutron production, there are many possible reactions (cf. Table 1.1), each offering different possibilities. In order to examine why the ^{7}Li(p, n)^{7}Be reaction is used at the FRANZ facility, the aims and limitations of the Frankfurt neutron source project need to be considered. Because of the technical challenges involved, gas and unstable targets are not used (eliminating ^{3}H, ^{15}N, ^{36}Cl, and ^{39}Ar). Additionally, for tritium very high safety precautions would be required due to its high toxicity. Operational safety also discourages the use of ^{6}Li and ^{12}C: protons would need to be accelerated to higher energies, so secondary particles (e.g. electrons) would also have higher energies, thus necessitating improved radiation protection. Additionally, higher energies are connected to higher power consumption, so better high-frequency transmitters would be required increasing the investment costs. Using the ^{13}C isotope for the target would also mean higher costs because of its low relative abundance of only 1.1 % [21]. The remaining carbon isotope, ^{14}C, as

reaction	threshold energy
^{3}H(p, n)^{3}He	1.0191 MeV
^{6}Li(p, n)^{6}Be	5.9223 MeV
^{7}Li(p, n)^{7}Be	1.8807 MeV
^{7}Li(p, n)^{7}Be*	2.3714 MeV
^{9}Be(p, n)^{9}B	2.0578 MeV
^{10}Be(p, n)^{10}B	0.2496 MeV
^{10}B(p, n)^{10}C	4.8774 MeV
^{11}B(p, n)^{11}C	3.0187 MeV
^{12}C(p, n)^{12}N	19.657 MeV
^{13}C(p, n)^{13}N	3.2363 MeV
^{14}C(p, n)^{14}N	0.6714 MeV
^{15}N(p, n)^{15}O	3.7748 MeV
^{36}Cl(p, n)^{36}Ar	0.07757 MeV
^{39}Ar(p, n)^{39}K	0.2248 MeV
^{59}Co(p, n)^{59}Ni	1.8897 MeV

Table 1.1.: Neutron production reactions suitable for acelerator-based neutron sources [22].

well as ^{10}Be are unstable – since the BaF$_2$ detector used in the time-of-flight setup is sensitive to radiation, unstable targets would cause an unnecessary background in measurements and therefore degrade the spectrum.

Comparing the cross sections above the threshold for the remaining six candidates (cf. Figure 1.6), it is evident that the ^{7}Li(p, n)^{7}Be reaction offers a cross section approximately four times larger than that of ^{9}Be(p, n)^{9}B motivating its application at FRANZ.

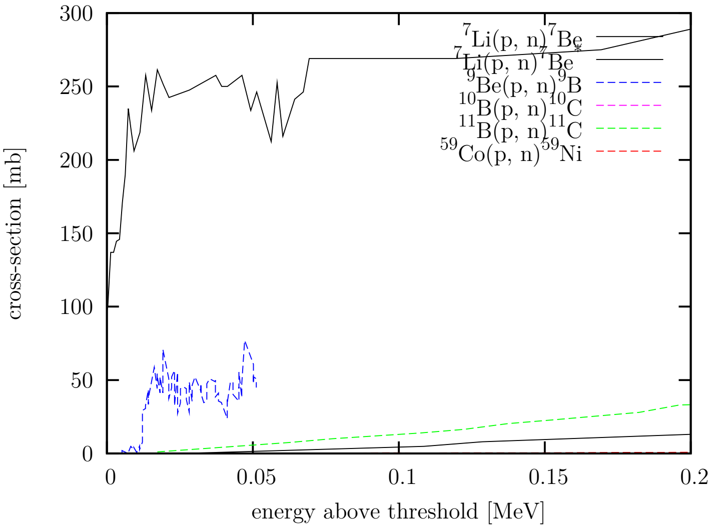

Figure 1.6.: Comparison of the neutron production cross sections in different reactions. The cross sections were taken from: ^{7}Li(p, n)^{7}Be and ^{7}Li(p, n)^{7}Be*: [23], ^{9}Be(p, n)^{9}B: [24], ^{10}B(p, n)^{10}C: [25], ^{11}B(p, n)^{11}C: [26], ^{59}Co(p, n)^{59}Ni: [27].

1.3. The ^{7}Li(p, n)^{7}Be reaction

1.3.1. Compound nucleus reaction

In the lithium-beryllium reaction, the incoming protons react with ^{7}Li forming an intermediate ^{8}Be nucleus. In numerous nucleon-nucleon collisions, the binding energy released by absorbing the incident particle is distributed among the nucleons – the probability for a single nucleon to carry the whole energy is small. The compound nucleus state is entered if the system reaches thermal equilibrium [28, p. 331]. This state generally lasts longer than the passing time of the incident particle would be. In case of the ^{7}Li(p, n)^{7}Be reaction, the intermediate ^{8}Be nucleus decays after approximately $\tau_{\mathrm{decay}} \approx 200 \times 10^{-15}\,\mathrm{s}$ [29, p. 74], while the passing time is $\tau_{\mathrm{passing}} = d_{^{8}\mathrm{Be}}/v_{\mathrm{p}} \approx 10^{-22}\,\mathrm{s}$ (for $E_{\mathrm{p}} = 2\,\mathrm{MeV}$). Here, $d_{^{8}\mathrm{Be}}$ denotes the diameter of the nucleus and v_{p} is the proton velocity.

Because of the statistical distribution of the excitation energy among the nucleons, the system loses information about its formation. Therefore, the decay of the state is decoupled from its creation, so the neutron beam properties are almost independent of the proton beam properties. Of course, a major exception is the energy, as in the process of de-excitation the intermediate nucleus transfers its energy to the emitted particle [30, cf. p. 150].

1.3.2. Threshold

The ^{7}Li(p, n)^{7}Be reaction exhibits a threshold energy at which neutron production starts. Based on the nuclear masses, this energy has been determined with great accuracy [31] to

$$E_{\text{thresh}}^{\text{exp}} = (1.880443 \pm 0.000020)\,\text{MeV} \tag{1.4}$$

The value can be reproduced by evaluating the reaction using energy and momentum conservation. In special relativity, one can exploit the fact that scalar values do not depend on the reference frame. Therefore, the inital state, described in the lab frame, can be compared to the final state, described in the center of mass frame (CM frame)

$$\underbrace{(P_{\text{p}} + P_{\text{Li}})}_{\text{lab frame}}{}^2 = \underbrace{(P_{\text{n}} + P_{\text{Be}})}_{\text{CM frame}}{}^2 \tag{1.5}$$

where

$$P_{\text{p}} = \begin{pmatrix} E_{\text{p}}/c + m_{\text{p}}c \\ \vec{p}_{\text{p}} \end{pmatrix} \qquad P_{\text{Li}} = \begin{pmatrix} m_{\text{Li}}c \\ \vec{0} \end{pmatrix} \tag{1.6a}$$

$$P_{\text{n}} = \begin{pmatrix} m_{\text{n}}c \\ \vec{0} \end{pmatrix} \qquad P_{\text{Be}} = \begin{pmatrix} m_{\text{Be}}c \\ \vec{0} \end{pmatrix} \tag{1.6b}$$

The neutron production threshold is characterized by the fact that the total energy in the center of mass frame is just $E_{\text{CM}} = m_{\text{n}}c^2 + m_{\text{Be}}c^2$: There is no more energy left for motion relative to the center of mass. For this reason, the particle momenta in (1.6b) are $\vec{0}$, so $E_{\text{p}} = E_{\text{thresh}}$.

Insertion of (1.6) into (1.5) and use of the relation $P^2 = m^2c^2$ yields

$$m_{\text{p}}^2c^2 + 2\begin{pmatrix} E_{\text{thresh}}/c + m_{\text{p}}c \\ \vec{p}_{\text{p}} \end{pmatrix}\begin{pmatrix} m_{\text{Li}}c \\ \vec{0} \end{pmatrix} + m_{\text{Li}}^2c^2 = m_{\text{n}}^2c^2 + 2\begin{pmatrix} m_{\text{n}}c \\ \vec{0} \end{pmatrix}\begin{pmatrix} m_{\text{Be}}c \\ \vec{0} \end{pmatrix} + m_{\text{Be}}^2c^2$$
$$m_{\text{p}}^2c^2 + 2\left(E_{\text{thresh}} + m_{\text{p}}c^2\right) m_{\text{Li}} + m_{\text{Li}}^2c^2 = m_{\text{n}}^2c^2 + 2\,m_{\text{n}}c\,m_{\text{Be}}c + m_{\text{Be}}^2c^2$$

Solving for the threshold energy E_{thresh} gives

$$E_{\text{thresh}} = \frac{1}{2\,m_{\text{Li}}}\left((m_{\text{n}}^2 + m_{\text{Be}}^2 - m_{\text{p}}^2 - m_{\text{Li}}^2)\,c^2 + 2\,m_{\text{n}}c\,m_{\text{Be}}c\right) - m_{\text{p}}c^2 \tag{1.7}$$

Finally, with the nuclear masses [32]

$$m_{\text{p}} = 938.27198\,\frac{\text{MeV}}{\text{c}^2} \qquad m_{\text{n}} = 939.56533\,\frac{\text{MeV}}{\text{c}^2}$$
$$m_{\text{Li}} = 6\,533.83324\,\frac{\text{MeV}}{\text{c}^2} \qquad m_{\text{Be}} = 6\,534.18413\,\frac{\text{MeV}}{\text{c}^2}$$

the threshold energy can be determined to be

$$E_{\text{thresh}} = 1.880563\,\text{MeV}$$

Note the small difference to the measured value in (1.4), which probably results from differing nuclear mass data.

If protons exceed the aforementioned threshold energy significantly, the ^{7}Be nucleus can be excited to the $E^* = 0.42908\,\text{MeV}$ [29] level. If excited, this state is a second source of neutrons via the $^7\text{Li}(\text{p, n})^7\text{Be}^*$ reaction. Since a certain fraction of the proton's energy is required for the excitation, these neutrons have less kinetic energy than neutrons from the ground state. By replacing m_{Be} with $m_{\text{Be}^*} = m_{\text{Be}} + E^*/c^2$ in (1.7), the threshold energy for this level can be calculated to be

$$E^*_{\text{thresh}} = 2.371382\,\text{MeV}$$

making it irrelevant if proton energies only range up to 2.2 MeV (e.g. FRANZ, cf. Figure 1.3).

1.3.3. Kinematic collimation

Another feature of this neutron production reaction is the kinematic collimation. In the lab frame, neutrons are not emitted in every direction, but instead they are focused in a cone with an opening angle depending on the proton energy. As long as the neutron velocity in the center of mass system is lower than the velocity of the center of mass itself, i.e. $|\vec{v}_{\text{CM}}|$ dominates $|\vec{v}_{\text{n}}^{\text{CM}}|$ in

$$\vec{v}_{\text{n}} = \vec{v}_{\text{n}}^{\text{CM}} + \vec{v}_{\text{CM}} \qquad \text{cf. (A.11)}$$

the emission angle θ remains below 180°: Even if the neutron is emitted backwards in the center of mass system (the actual angle is given statistically by $\mathrm{d}\sigma/\mathrm{d}\Omega$), the sum of $\vec{v}_{\text{n}}^{\text{CM}}$ and $\vec{v}_{\text{CM}}$ points at 0°. For other emission angles in the center of mass system, the $\vec{v}_{\text{CM}}$ component modifies the emission angle similarly leading to the collimation of the neutron beam. At $E_{\text{p}} = 1.912\,\text{MeV}$ this effect leads to a cone with 120° opening angle corresponding to a maximum emission angle of 60°.

The equation above also shows another feature of the reaction: At $E_{\text{p}} = E_{\text{thresh}}$, the neutron kinetic energy is not zero. The available energy in the center of mass is just enough to produce a neutron at rest, i.e. $\vec{v}_{\text{n}}^{\text{CM}} = \vec{0}$ but due to momentum conservation the center of mass velocity $\vec{v}_{\text{CM}}$ is not $\vec{0}$. Therefore

$$\vec{v}_{\text{n}} \neq \vec{0}$$

the kinetic energy is not zero, but $\approx 30\,\text{keV}$.

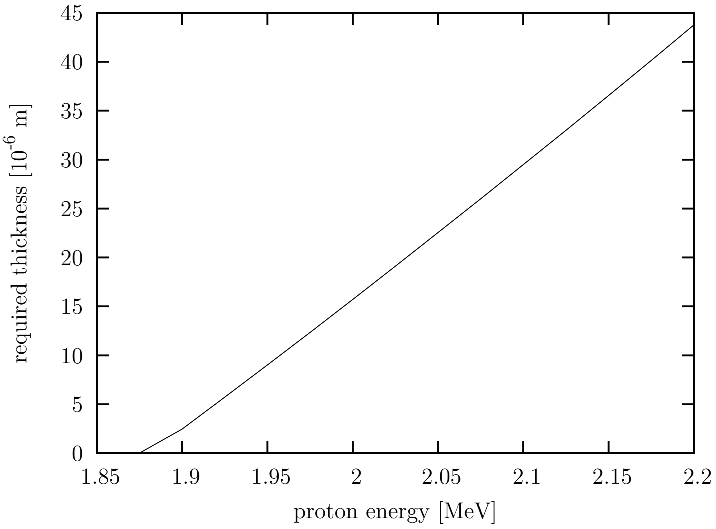

Figure 1.7.: ^{7}Li thickness required to slow down protons of a given energy to energies below the neutron production threshold (based on SRIM [33] data).

1.3.4. Particle stopping

While not being a specialty of the ^{7}Li(p, n)^{7}Be reaction, the stopping of incident particles in the target results in important effects on the neutron spectrum. Since the required thickness to slow down protons to energies below the production threshold is rather low (only 4 µm at $E_\mathrm{p} = 1.912\,\mathrm{MeV}$, cf. Figure 1.7), protons with an initial energy of $E_\mathrm{p} = 1.912\,\mathrm{MeV}$ will slow down to threshold energy in a 10 µm thick target [19].

2. Implementation

2.1. Requirements

In order to analyze the transformation of beam properties, the simulation code "n17" has been developed, which is able to handle six-dimensional proton data – that is, three spatial and three velocity dimensions. Since the behaviour of a (drifting) particle beam is determined by its constituents, every beam parameter can be derived from and expressed in terms of the distribution of single particles. Therefore, this input format provides maximum information for a beam, while also permitting tests with monoenergetic beams or different beam diameters to investigate different levels of target irradiation.

To retain as much information as physically possible, the code outputs neutron data in the same format. These data can then be used to analyze the transformation of beam properties, or they can be used in the framework of the FRANZ project to simulate the reaction inside the neutron sample and, subsequently, the detector response. In this context, the code can be incorporated into an end-to-end simulation of the whole accelerator, starting at the ion source and ending in the detector feedback. By combining this simulation with an optimization algorithm, e.g. the particle swarm algorithm as suggested in [34], it would be possible to find the best accelerator settings for a given experiment. Additionally, a full simulation might help experimentalists to confirm that given setups work as expected.

The output beam properties depend on the target shape – in curved targets for example, the thickness for protons of a coplanar beam will differ. So even if the particles had the same initial energy, they would not pass through the same thickness. Therefore, the simulation program was designed to not put any constraints on the target shape allowing the investigation of solid targets as in FRANZ [19] as well as liquid targets favoured by other research groups [35].

2.2. Proton representation

In high neutron flux experiments like FRANZ, proton pulses are comprised of more than 10^{10} particles (see (1.3)) when hitting the target. If every proton was simulated as a single entity and one calculation took only 1 ms, a simulation of the whole bunch interaction would still take $4.815 \times 10^{7}\,\mathrm{s} \approx 1.5\,\mathrm{years}$. In order to reduce the computation complexity, multiple protons are combined into a single simulated particle. For ease of reference, this type of particle will be called "$\mathcal{P}$ particle". A $\mathcal{P}$ particle has a single location and velocity vector, yet it knows the number of protons it is comprised of – it may be considered as the center of mass of the protons it consists of.

In n17, the number of $\mathcal{P}$ particles is determined by the number of particles given in the input file, N_{input}. Every tuple of location and velocity vector is considered a $\mathcal{P}$ particle each of which represents $N_{\mathrm{p}}/N_{\mathrm{input}}$ protons (N_{p} as calculated in (1.3)). That is, increasing the number of input particles improves the precision of the simulation but it also increases computation time and memory requirements, yet it does not increase the total charge impinging on the target.

2.3. Space charge

In general, the proton input data describe a bunch of particles with finite extent. With pulses of a few centimeters length ($l = 1.57\,\mathrm{cm}$ at $E_{\mathrm{p}} = 2.0\,\mathrm{MeV}$), a full simulation cannot assume that all bunch particles pass through the target at once. Therefore, even if the input data are generated so that the frontmost particle of the whole bunch already touches the target, n17 must be capable of transporting the remaining particles.

As a proton moves to the surface, it is continuously exposed to a repelling field caused by other protons. The maximum transversal momentum deviation caused by this field can be estimated by considering the bunch as a sphere with a charge equal to the charge of the proton bunch (cf. Figure 2.1). The point charge $q = e$ at $d = 6\,\mathrm{mm}$ represents the proton that is exposed to the repelling field of the sphere. The distance of 6 mm is the expected root-mean-square (rms) radius of a proton bunch at $E_{\mathrm{p}} = 2.0\,\mathrm{MeV}$ just in front of the ^{7}Li target.

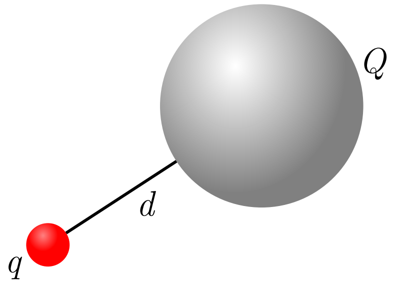

Figure 2.1.: Model to estimate the momentum deviation.

To calculate the maximum deviation, the proton is assumed to be subject to the forces for the time

$$t = \frac{l}{v_\mathrm{p}} = l\sqrt{\frac{m_\mathrm{p}}{2E_\mathrm{p}}}$$

Throughout this time, the force is lower than

$$F = \frac{1}{4\pi\,\epsilon_0}\frac{q\,Q}{d^2} \tag{2.1}$$

because d actually increases because of the Coulomb force (2.1) according to

$$F = m_\mathrm{p} a = m_\mathrm{p}\ddot{d} \tag{2.2}$$

Instead of solving (2.1) together with (2.2), a constant repelling acceleration of $a = \frac{F}{m_\mathrm{p}}$ is assumed, yielding a momentum deviation of

$$p_\mathrm{T} = m_\mathrm{p}\,(a\,t) = t\,F \tag{2.3}$$

Together with $Q_\text{at-target} = 7.7143 \times 10^{-9}\,\mathrm{C}$ from (1.2), equation (2.1) yields

$$F = 3.09 \times 10^{-13}\,\mathrm{N}$$

corresponding to

$$\begin{aligned} p_\mathrm{T} &= t\,F \\ &= l\sqrt{\frac{m_\mathrm{p}}{2E_\mathrm{p}}}\,F \\ &= 1.57\,\mathrm{cm}\sqrt{\frac{938\,\frac{\mathrm{MeV}}{\mathrm{c}^2}}{2\times 2\,\mathrm{MeV}}}\,3.09\times 10^{-13}\,\mathrm{N} \\ &= 463\,\frac{\mathrm{keV}}{\mathrm{c}} \end{aligned} \tag{2.4}$$

In comparison to the longitudinal momentum $p_\mathrm{L} = \sqrt{2\,m_\mathrm{p}\,E_\mathrm{p}} = 61\,253\,\frac{\mathrm{keV}}{\mathrm{c}}$, p_T is negligible.

Moreover, the space charge forces will be modified when the proton beam hits the target surface. Many secondary particles will be created, with electrons being the most dominant species. The negative charges will be attracted by the positive beam potential and eventually cancel out the beam space charge in the vicinity of the target surface. Inside the target, the space charge field is modified by the metallic lithium. For a given proton, this modification is only relevant for a short time because firstly, the target is very thin (current designs aim at a thickness of 10 µm) and secondly, after the ^{7}Li(p, n)^{7}Be reaction has taken place, the resulting neutron is not affected by space charge effects as it does not carry a charge itself.

Summarizing the above considerations, it is yet to be studied how space charges are screened in front of and within the ^{7}Li target, while unscreened space charge forces only cause a small error. Therefore, n17 does not simulate space charge effects. Instead, it only translates protons until they reach the target.

This enables an optimization path because the time it takes for protons to reach the target can be calculated by solving a linear equation. Therefore, time stepping only has to be used inside the target.

2.4. Time steps and target thickness

Each proton is transported in time steps of $\Delta t = 10^{-15}\,\mathrm{s}$ when inside the target, corresponding to a distance of $v\,\Delta t \approx 0.02\,\mu\mathrm{m}$ for $E_\mathrm{p} = 2\,\mathrm{MeV}$. The passed thickness inside the target material between two time steps, Δx, is required to calculate energy loss as well as the probability for neutron production (see section 2.5, "Interaction probability and scattering direction").

In a simple implementation, one might assume Δx to be $v\,\Delta t$ as long as the proton is inside the target and zero otherwise. This may produce sufficiently good results for small Δt, but the target's longitudinal extent may be wrongly estimated: Assuming that the current time step positioned the proton immediately behind the target's rear boundary, the target will be simulated as if it was almost $v\,\Delta t$ smaller since the proton is now outside and – as specified above – this results in a passed thickness of zero. A major problem of this approach is its energy dependency. Since different E_p lead to different velocities which in turn result in different step lengths $v\,\Delta t$, the target size would be simulated to depend on the proton energy. In Figure 2.2, this scenario is described by the orange dotted line.

The black line depicts the current implementation. There, the distance passed between two steps is computed from the target geometry. For cylindrical targets, there are four cases:

1. In the previous and in the current step, the proton is inside the target. Hence the thickness passed is the distance between both positions.

2. The particle did not pass the target, so the thickness is 0.

3. In one of both steps the particle was inside the target, while in the other one it was outside.

4. The particle entered and exited the target completely between two steps.

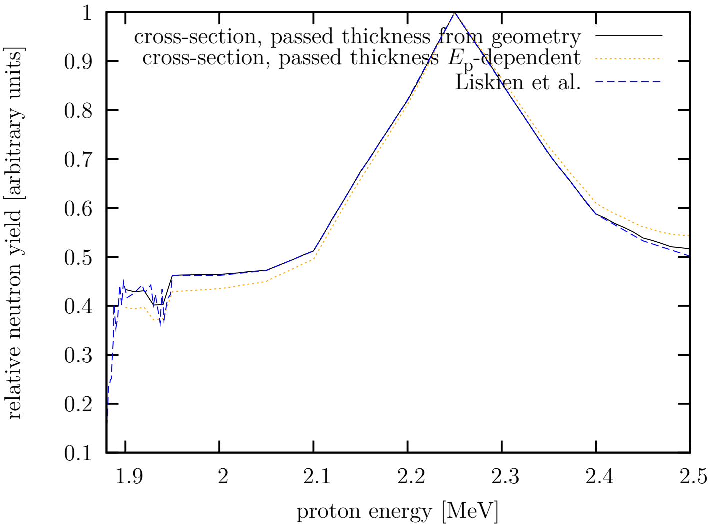

Figure 2.2.: Neutron yield for different thickness evaluation methods (black and orange, see text), compared to the reference data in blue; time steps of $\Delta t = 10^{-12}\,\mathrm{s}$, proton energy resolution set to $\Delta E_\mathrm{p} = 10\,\mathrm{keV}$. Since all curves are normalized to their maxima, the deviation of the orange line from the reference data increases as the energy difference to $E_\mathrm{max} \approx 2.25\,\mathrm{MeV}$ increases.

Cases three and four are the most difficult cases. To calculate the thickness for them, it is convenient to describe the particle trajectory using

$$\vec{r}(\lambda) = \vec{r}_1 + \underbrace{(\vec{r}_2 - \vec{r}_1)}_{\Delta\vec{r}}\,\lambda \tag{2.5}$$

where the particle position in the different steps is given by $\vec{r}_1$ and $\vec{r}_2$ and $\lambda \in [0,1]$ being an arbitrary parameter. For cases 3 and 4, there are four possible intersections of $r(\lambda)$ with the cylinder: one with the base, one with the cap and two with the barrel. If the cylinder's symmetry axis is positioned along the x axis, the intersection with base and cap are only possible if $(\Delta\vec{r})_x \neq 0$. Then, the corresponding λ values can be calculated using

$$\lambda_1 = \frac{1}{(\Delta\vec{r})_x}\Big(x_{\text{base}} - (\vec{r}_1)_x\Big) \qquad \lambda_2 = \frac{1}{(\Delta\vec{r})_x}\Big(x_{\text{cap}} - (\vec{r}_1)_x\Big)$$

For the barrel, the equation

$$r_{\text{cyl}}^2 = \Big((\vec{r}_1)_y + (\Delta\vec{r})_y\,\lambda\Big)^2 + \Big((\vec{r}_1)_z + (\Delta\vec{r})_z\,\lambda\Big)^2$$

can provide up to two more λ values. Obviously, any $\lambda \notin [0,1]$ describes points that have not been passed between the two steps (cf. (2.5)), so the respective solutions have to be discarded. If there is no λ left, the line given by (2.5) does not intersect the cylinder at all, resulting in a passed thickness of zero. Else, the distance d is given by

$$d = \vec{p}_2 - \vec{p}_1$$

with

$$\vec{p}_1 = \begin{cases} \vec{r}_1 & \text{if } r_1 \text{ is inside the target} \\ \vec{r}(\lambda_{\text{min}}) & \text{else} \end{cases}$$

$$\vec{p}_2 = \begin{cases} \vec{r}_2 & \text{if } r_2 \text{ is inside the target} \\ \vec{r}(\lambda_{\text{max}}) & \text{else} \end{cases}$$

and

$$\lambda_{\text{min}} = \min\{\lambda_i\} \qquad \lambda_{\text{max}} = \max\{\lambda_i\}$$

2.5. Interaction probability and scattering direction

Generally, only a certain fraction of the incoming beam actually reacts in the ^{7}Li(p, n)^{7}Be reaction. This fraction is expressed in terms of the cross section value, the apparent cross-sectional area of the target nucleus for the reaction. The probability for a single proton to react in dx is given by

$$\mathrm{d}P = \rho\,\sigma\,\mathrm{d}x \tag{2.6}$$

where σ denotes the cross section, and ρ stands for the target density (atoms per volume). When calculating the reaction probability along x, one has to take into account that the proton may disappear and therefore does not react anymore in later steps. This results in the differential equation

$$\mathrm{d}P = (1 - P)\,\rho\,\sigma\,\mathrm{d}x$$

which can be solved using the initial condition $P(x = 0) = 0$:

$$\begin{aligned}\int\limits_0^P \frac{1}{1-P'}\,\mathrm{d}P' &= \int\limits_0^x \rho\,\sigma\;\mathrm{d}x' \\ P &= 1 - \exp(-\rho\,\sigma\,x) \qquad (2.7)\end{aligned}$$

Equation (2.7) corresponds to the well-known formula $R = I\ (1 - \exp(-\rho\,\sigma\,x))$ with $P = R/I$, the number of reactions per incoming particle.

Every time step, the n17 code calculates the probability for a reaction in the current step according to

$$\begin{aligned}\Delta P &= \frac{\mathrm{d}P}{\mathrm{d}x}\,\Delta x \\ &= \rho\,\sigma\,\Delta x \quad \text{compare (2.6)} \qquad (2.8)\end{aligned}$$

where $\sigma = \sigma(E_\mathrm{p})$, the energy-dependent cross section, is taken from [23]. Δx denotes the length the proton travelled since the previous time step.

The probability ΔP is compared to a random value $k \in [0, 1]$. If $k > \Delta P$, the proton passes on. Otherwise, the reaction is assumed to take place. In order to determine the scattering angle in the center of mass system, the angular probability distribution

$$\begin{aligned}P_\text{angular}(\theta^\text{CM}) &\propto \left(\frac{\mathrm{d}\sigma}{\mathrm{d}\Omega}\right)^\text{CM} \Delta\Omega^\text{CM} \\ &= \left(\frac{\mathrm{d}\sigma}{\mathrm{d}\Omega}\right)^\text{CM} 2\pi\,\sin(\theta^\text{CM})\,\Delta\theta^\text{CM}\end{aligned}$$

is calculated with $\left(\frac{\mathrm{d}\sigma}{\mathrm{d}\Omega}\right)^\text{CM} = \left(\frac{\mathrm{d}\sigma}{\mathrm{d}\Omega}\right)^\text{CM}(E_\mathrm{p}, \theta^\text{CM})$, i.e. the differential cross section is a function of the proton kinetic energy E_p and the scattering angle θ^CM. As an example, the distribution for 2.0 MeV is shown in Figure 2.3. While it is not difficult

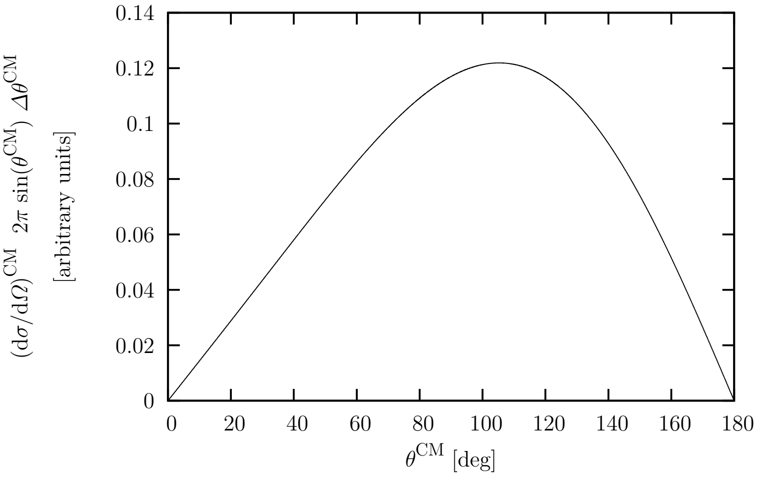

Figure 2.3.: Angular probability distribution of the ^{7}Li(p, n) reaction for 2 MeV proton energy.

to homogenously choose a value from a given numerical interval, there is no easy means of choosing a value according to the probability distribution described above. Therefore, the function is transformed – first, it is split up into N x-y pairs. Each pair i is assigned a sub-interval in $[0, 1)$ the size of which is equal to the relative probability

$$P_i = \frac{y_i}{\sum\limits_{j=1}^{N} y_j}$$

and ranges from

$$I_i = \left[\sum_{j=1}^{i-1} P_j, P_i + \sum_{j=1}^{i-1} P_j\right)$$

Then, if a random value ℓ homogenously from $[0, 1)$ fulfills the condition $\ell \in I_i$, y_ℓ will be chosen correctly according to the distribution.

2.6. Kinetic energy and transformation

After θ^{CM}, the angle between the incident proton trajectory and the produced neutron direction in the center of mass system, has been determined, the kinetic energy of the emitted neutron is calculated according to appendix A. Together with θ^{CM} and a random angle $\phi \in [0, 2\pi]$, the components of the velocity vector v_x, v_y, and v_z in the lab system are fixed when using the angle transformation given in [36].

Since in general the proton direction is not parallel to one of the lab frame axes, the neutron velocity vector has to be converted to the lab system.

In order to generate the transformation matrix from the "proton system" $\mathcal{S}$ to the lab system $\mathcal{L}$, three base vectors $\vec{b}_1$, $\vec{b}_2$, $\vec{b}_3$ are necessary. They are generated from the normalized proton velocity vector $\vec{v}' = \vec{v}/v$ according to

$$\begin{aligned}\vec{b}_1 &= \vec{v}' \\ \vec{b}_2 &= \begin{cases}\vec{y} & \text{if } \vec{y} \times \vec{v}' \neq \vec{0} \\ \vec{z} & \text{if } \vec{y} \times \vec{v}' = \vec{0}\end{cases} \\ \vec{b}_3 &= \vec{b}_1 \times \vec{b}_2\end{aligned}$$

The vectors are not orthonormalised yet, so the Gram-Schmidt process helps obtain new base vectors $\vec{b}_1'$, $\vec{b}_2'$, $\vec{b}_3'$, which are then used to calculate the transformation matrix

$$M = \begin{pmatrix} b'_{1,x} & b'_{2,x} & b'_{3,x} \\ b'_{1,y} & b'_{2,y} & b'_{3,y} \\ b'_{1,z} & b'_{2,z} & b'_{3,z} \end{pmatrix}$$

Finally, this matrix can be applied to get the neutron direction in the lab system, $\vec{v}_\mathrm{n}^{\mathcal{L}\,\prime}$

$$\vec{v}_\mathrm{n}^{\mathcal{L}\,\prime} = M\,\vec{v}_\mathrm{n}^{\mathcal{S}\,\prime}$$

2.7. Target description

As outlined in section "Requirements" (section 2.1), the target description is very general requiring only a handful of definitions common to any solid or liquid target. First of all, the target's density ρ is required to calculate the interaction probability according to section 2.5. Its geometric properties are covered by three distinct functions. The first function defines a bounding box, the smallest cuboid by which the whole target is enclosed. If a particle is outside this box, any possibly complex tests concerning the geometric details of the target are skipped. If a particle is inside this box, the implementation of the target must be capable of evaluating whether a given three-dimensional coordinate is actually inside the target and not just inside its bounding box. With this specification, it would already be possible to determine the passed thickness, thus satisfy the considerations of section 2.4, which require this information. However, this would be a slow process prone to introduce numerical errors as the number of queries is finite. Therefore, a different routine is required to calculate the thickness of lithium between to different positions taking into account the geometry of the target that is to be implemented.

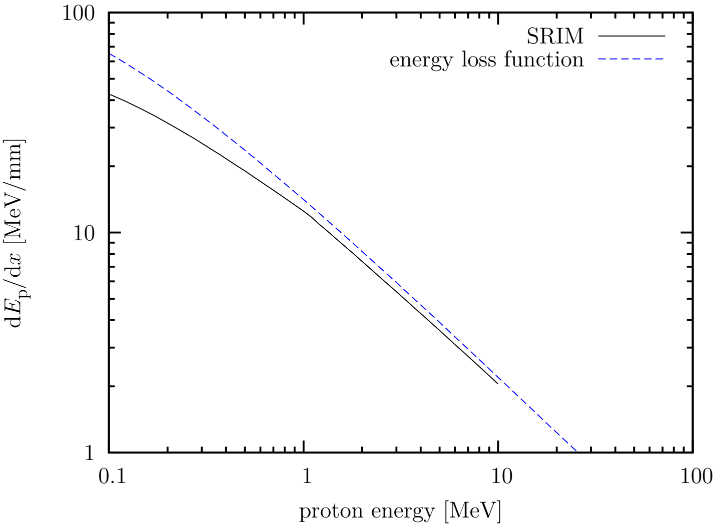

Figure 2.4.: The stopping power of protons inside ^{7}Li as simulated using SRIM. For comparison, the Bethe-Bloch energy loss function (2.9) is given. Especially in the low energy region these functions differ significantly.

2.8. Particle stopping

If a simulated proton is not converted into a neutron in a given time step, it is simulated to slow down. The energy loss of a single time step is calculated according to

$$E_\mathrm{loss} = \frac{\mathrm{d}E}{\mathrm{d}x}\,\Delta x$$

As in (2.8), Δx stands for the thickness passed in the last time step. The energy loss function $\frac{\mathrm{d}E}{\mathrm{d}x}(E)$ used in n17 has been calculated using the SRIM code [33]. It uses a Monte Carlo based approach to compute the function, so it does not directly rely on the Bethe-Bloch energy loss function

$$-\frac{\mathrm{d}E}{\mathrm{d}x} = \left(\frac{1}{4\pi\epsilon_0}\right)^2 \frac{4\pi\, q^2\, Q^2\, n_\mathrm{e}}{m_\mathrm{e}c^2\,\beta^2}\left[\ln\left(\frac{2\,m_\mathrm{e}c^2\,\gamma^2\beta^2}{I}\right) - \beta^2\right] \tag{2.9}$$

In Figure 2.4, the latter function is plotted side by side with the SRIM results. Obviously, Bethe's formula overestimates the stopping power in the low energy regime that is very important for the simulation as the proton energy does not exceed 2 MeV.

2.9. Technical information

Tested environment

The n17 code can be compiled using g++-4.4 and runs on GNU/Linux (Ubuntu 10.10), although there are no strict dependencies on that platform. The code uses the Armadillo vector library[1] as well as some features from the Boost C++ library[2]; an optional graphical user interface is built using Qt[3].

File format

The input and output files of n17 contain six columns separated by tabs, each representing a numeric component of the position in six-dimensional space. Their meaning is as follows:

1. column: Position along the beam axis, commonly called z, in meters. Currently, the target's surface is assumed at $z = 0.3\,\mathrm{m}$.
2. column: Position along the x axis, which is one of the transversal axes, in meters.
3. column: Position along the y axis, the remaining transversal axis, in meters.
4. column: Velocity along the z axis, v_z, in meters per second.
5. column: Velocity along the x axis, v_x, in meters per second.
6. column: Velocity along the y axis, v_y, in meters per second.

This format neither uses momenta nor energies, thus avoiding the necessity to define the particle species. Instead, the input distribution is assumed to consist of $\mathcal{P}$ particles (see section 2.2), each of which is defined by a single valid line. Any line starting with a pound sign (`#`) is treated as a comment and is ignored by the program.

Additional tools supplement the core functionality of n17 by generating monoenergetic and gaussian input distributions or by creating angle-integrated diagrams, density plots and Mollweide projections.

---

[1] Armadillo version 0.9.60, `http://arma.sourceforge.net/`

[2] Boost version 1.42.0, `http://www.boost.org/`

[3] Qt version 4.7.0, `http://qt.nokia.com/`

3. Experiments

Comparing the simulated results with expectations and existing measurements can ensure that “n17” provides valid predictions for future experiments. In this thesis, the computed data are compared to measurements conducted at Forschungszentrum Karlsruhe and Physikalisch-Technische Bundesanstalt.

3.1. Expectations

The basic functionality of n17 can be verified by testing whether the simulation conforms to certain expectations. Most basically, the angle-integrated neutron count for a given proton energy E_p should be proportional to the cross section $\sigma(E_\mathrm{p})$ if stopping is irrelevant (“thin” target). In Figure 3.1, the prediction by the simulation (black line) is plotted together with the cross section data used for the calculation [23] (blue line). Both curves are normalized to their respective maxima, so apparently the simulated number of neutrons is proportional to the cross section data the simulation is based on.

The effects of kinematic collimation can be studied by using the Mollweide sphere projection [37, pp. 249–252]. It projects all (θ, ϕ) combinations from the spherical coordinate system onto a plane while maintaining the size relation of areas. For this thesis, the projection has been adopted to illustrate the angular emission properties of a given reaction using false colors to denote the number of neutrons per pixel. The analysis of the simulated neutron spectrum from protons at $E_\mathrm{p} = 1.912\,\mathrm{MeV}$ (cf. Figure 3.2) yields that the opening angle of the neutron cone is 120° (cf. Figure 3.2). This corresponds to the expectation given in section 1.3.3. At 0°, the neutron count is maximized because in the lab frame, the center of mass velocity vector is added to the neutron velocity vector. In the near-threshold regime, the former dominates the latter, so there are more neutrons at small emission angles. In a two-dimensional plot which only takes neutrons into account that were emitted in a cone with a small opening angle, this results in a steeply increasing number of neutrons near $E_\mathrm{p} = E_\mathrm{thresh}$ (cf. Figure 3.3).

Most of the plots in this thesis concentrate on the relative curve shape, but sometimes the absolute yield is also relevant. For this, the simulation code is able to calculate the neutrons-per-proton ratio which can be compared to reference data.

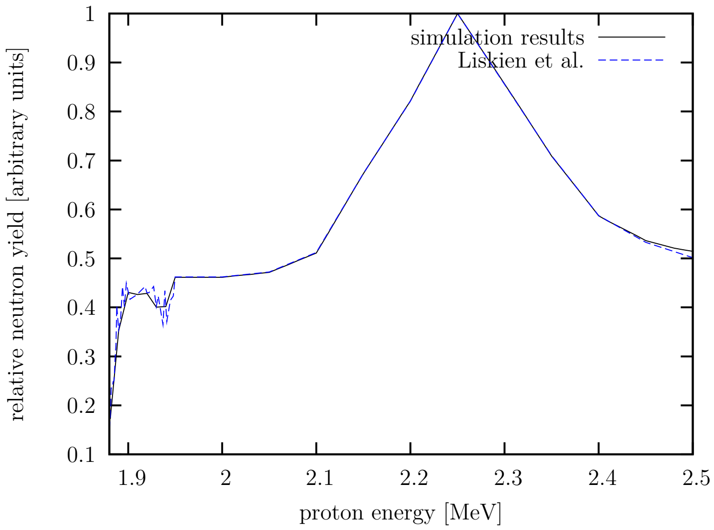

Figure 3.1.: Comparison of simulated yield with cross section, all curves are normalized to the maximum around 2.25 MeV.

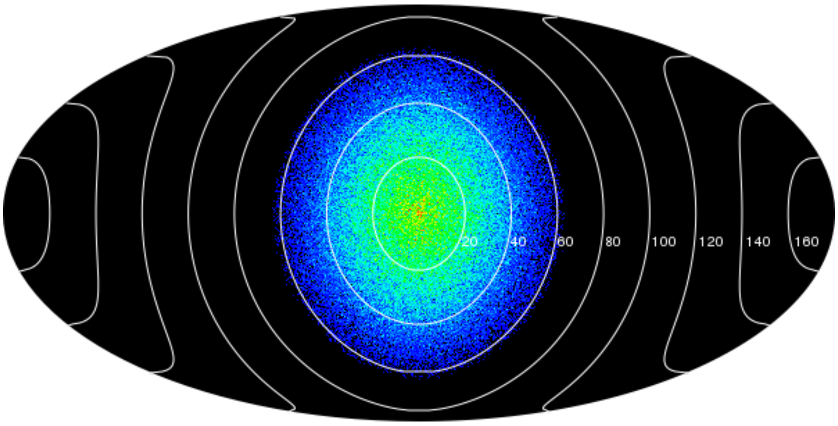

Figure 3.2.: Mollweide sphere projection of the emitted neutrons at 1.912 MeV. Red color denotes many neutrons in a given pixel, while blue stands for a low count. The coordinate system denotes the emission angles (cone opening angle divided by two) in degree.

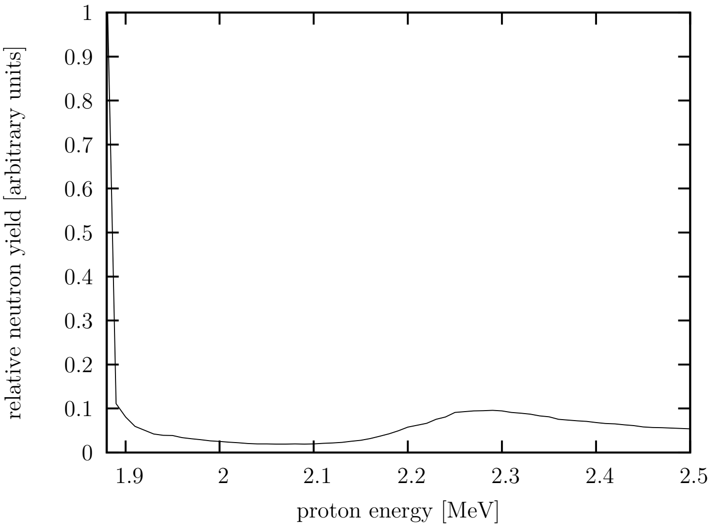

Figure 3.3.: Neutron yield in a cone of 5° opening angle in the lab frame.

Note that at FRANZ the proton count is fixed (see section 2.2) and therefore this ratio is equivalent to the number of neutrons itself. The shielding design [38] estimated the neutron flux for $E_\mathrm{p} = 2.2\,\mathrm{MeV}$ to be $1 \times 10^{-4}\,\frac{\mathrm{neutrons}}{\mathrm{proton}}$. As this should be a conservative estimation, n17 was expected to simulate a lower ratio. With a lithium layer thickness of $30\,\mu\mathrm{m}$, it predicts $4.5 \times 10^{-5}\,\frac{\mathrm{neutrons}}{\mathrm{proton}}$, which is close to the PINO [39] value of $4.7 \times 10^{-5}\,\frac{\mathrm{neutrons}}{\mathrm{proton}}$. For a layer thickness of only $10\,\mu\mathrm{m}$, the ratio is predicted to decrease to approximately $2 \times 10^{-5}\,\frac{\mathrm{neutrons}}{\mathrm{proton}}$ (n17: $1.9 \times 10^{-5}\,\frac{\mathrm{neutrons}}{\mathrm{proton}}$, PINO: $2.0 \times 10^{-5}\,\frac{\mathrm{neutrons}}{\mathrm{proton}}$) since there is not enough lithium to slow down protons below the threshold energy (cf. section 1.3.4).

3.2. Measurements at Forschungszentrum Karlsruhe

The experimental program at Forschungszentrum Karlsruhe (FZK) aimed at measuring the neutron capture cross sections of isotopes of astrophysical interest. There, it was most important to reproduce a Maxwellian distribution because the interaction data in temperature regions around 30 keV is required to properly model and predict the element synthesis in Red Giant stars. Therefore, the angle-integrated spectrum of the setup is well-known (cf. [40, p. 597]). Together with simulation predictions of n17 and PINO [39] the measurement data are plotted in Figure 3.5. For both codes a collinear proton beam with $E_\mathrm{p} = 1.912\,\mathrm{MeV}$ was used having an energy uncertainty of $\sigma = 1\,\mathrm{keV}$. Apparently, the agreement of both simulations is very good.

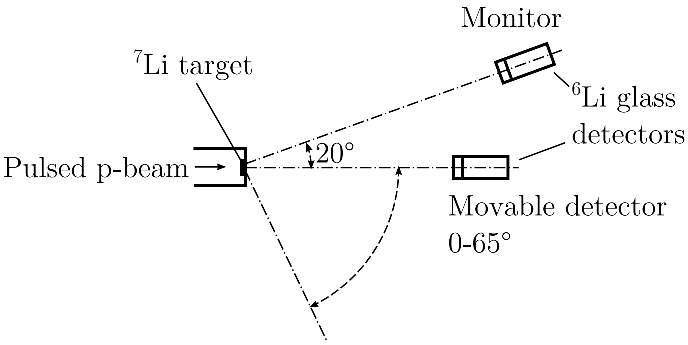

Figure 3.4.: Setup to measure the ^{7}Li(p, n)^{7}Be cross section at Forschungszentrum Karlsruhe [40].
Not to scale.

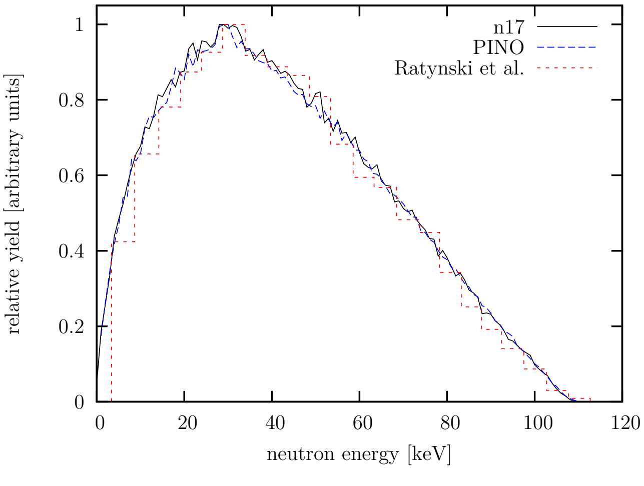

Figure 3.5.: Angle-integrated spectrum at $E_\mathrm{p} = 1.912\,\mathrm{MeV}$ ($\sigma = 1\,\mathrm{keV}$). The n17 simulation is compared to the PINO predictions [39] and measurement data taken from [40, p. 597].

The per-neutron analysis enables n17 to predict the spectra for different angles. When compared to measurements done in 1988 [41], the agreement is good for emission angles $\theta \geq 10°$ even though the simulation apparently underestimates the number of low-energetic neutrons (cf. Figure 3.5). At 0°, the code predicts a peak at 30 keV being the expected neutron energy for particles emitted by protons with $E_\mathrm{p} = E_\mathrm{thresh}$ (see discussion in section 1.3.3). As this feature is not visible in the experimental spectrum, it hints at a problem of the simulation. Since the predictions of n17 agree very well with other measurements and expectations, it seems plausible that this is a problem of the underlying data. Possibly, the cross section of the ^{7}Li(p, n) reaction close to the threshold is not known precisely enough – in fact, the determination of cross sections in this regime is very challenging as the proton energy uncertainty has to be small while at the same time the neutron detection must be very sensitive.

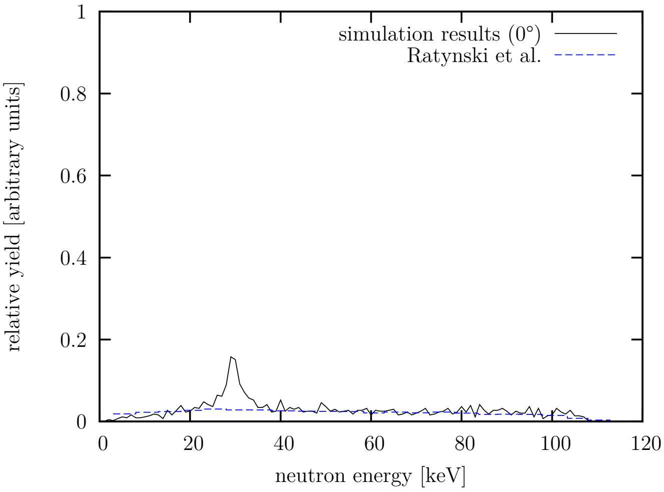
simulation results (0°)
Ratynski et al.
relative yield [arbitrary units]
neutron energy [keV]
0
0.2
0.4
0.6
0.8
1
0
20
40
60
80
100
120

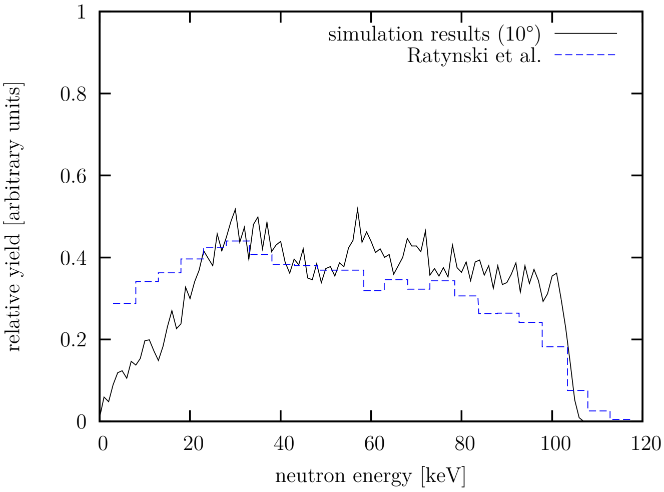
simulation results (10°)
Ratynski et al.
relative yield [arbitrary units]
neutron energy [keV]
0
0.2
0.4
0.6
0.8
1
0
20
40
60
80
100
120

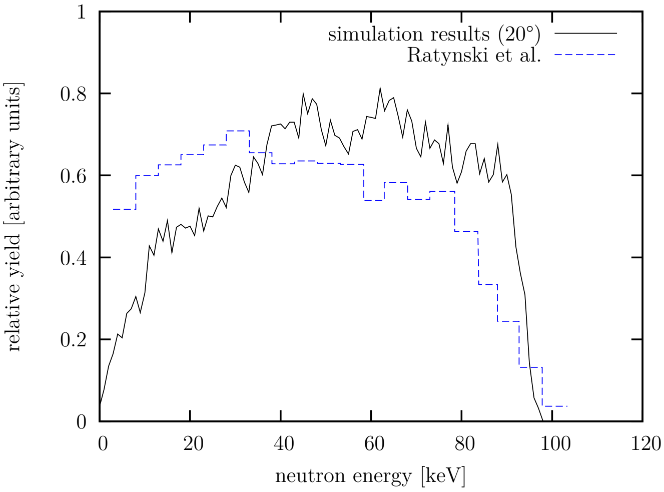
simulation results (20°)
Ratynski et al.
relative yield [arbitrary units]
neutron energy [keV]
0
0.2
0.4
0.6
0.8
1
0
20
40
60
80
100
120

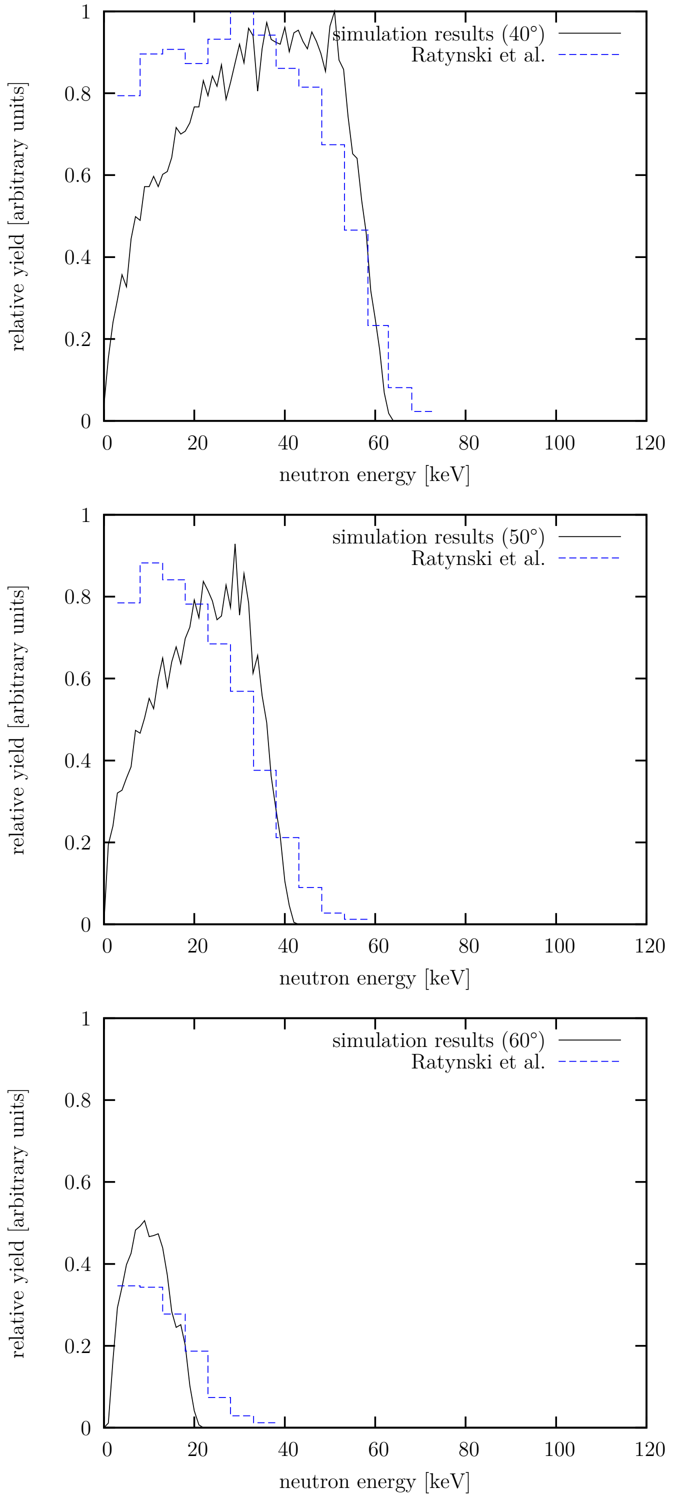

Figure 3.5.: Side-by-side comparison of simulated angular distributions with measurements conducted at Forschungszentrum Karlsruhe [41].

3.3. Measurements at Physikalisch-Technische Bundesanstalt

Recently, the cross section of the ^{7}Li(p, n)^{7}Be reaction was remeasured at Physikalisch-Technische Bundesanstalt (PTB) because of discrepancies of the Karlsruhe measurement to the so-called standard evaluation [42]. Even though in the latter experiment the detector is movable, the general setup is comparable to the setup at Forschungszentrum Karlsruhe and therefore capable of reproducing the experiment from 1988.

Preliminary results from the angular measurement are compared to the simulation (cf. Figure 3.7). Similar to the results from Karlsruhe, the prediction fits very well to the data for angles between 10° and 50°. In contrast to the FZK data, the PTB data show fewer low-energetic neutrons, thus the simulation matches the shape much better. The number of neutrons at higher energies, however, declines at lower values than predicted by n17 – in the FZK data the neutron count decreases at higher energies than in the simulation. Since the PTB data are still preliminary results, it is open to what extent possible changes will influence the agreement between the experimentally acquired data and the simulation.

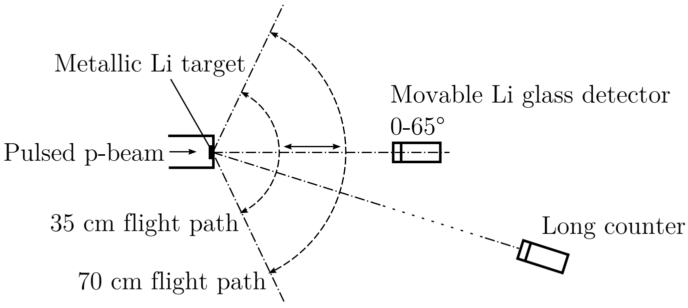

Figure 3.6.: Setup to measure the ^{7}Li(p, n)^{7}Be cross section at Physikalisch-Technische Bundesanstalt [43].
Not to scale.

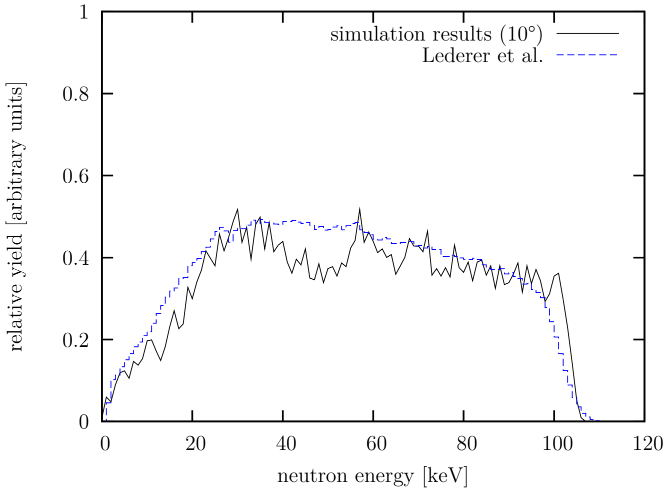
simulation results (10°)
Lederer et al.
relative yield [arbitrary units]
0
0.2
0.4
0.6
0.8
1
0
20
40
60
80
100
120
neutron energy [keV]

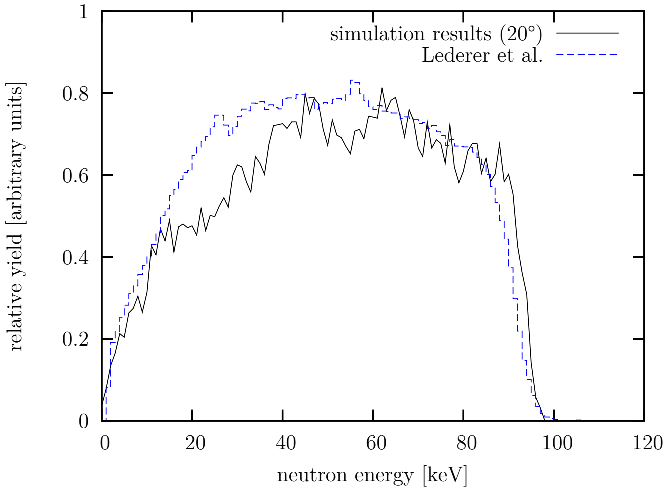
simulation results (20°)
Lederer et al.
relative yield [arbitrary units]
0
0.2
0.4
0.6
0.8
1
0
20
40
60
80
100
120
neutron energy [keV]

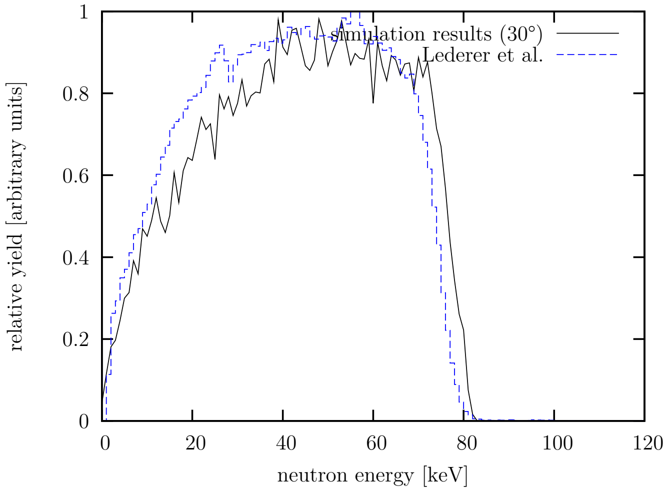
simulation results (30°)
Lederer et al.
relative yield [arbitrary units]
0
0.2
0.4
0.6
0.8
1
0
20
40
60
80
100
120
neutron energy [keV]

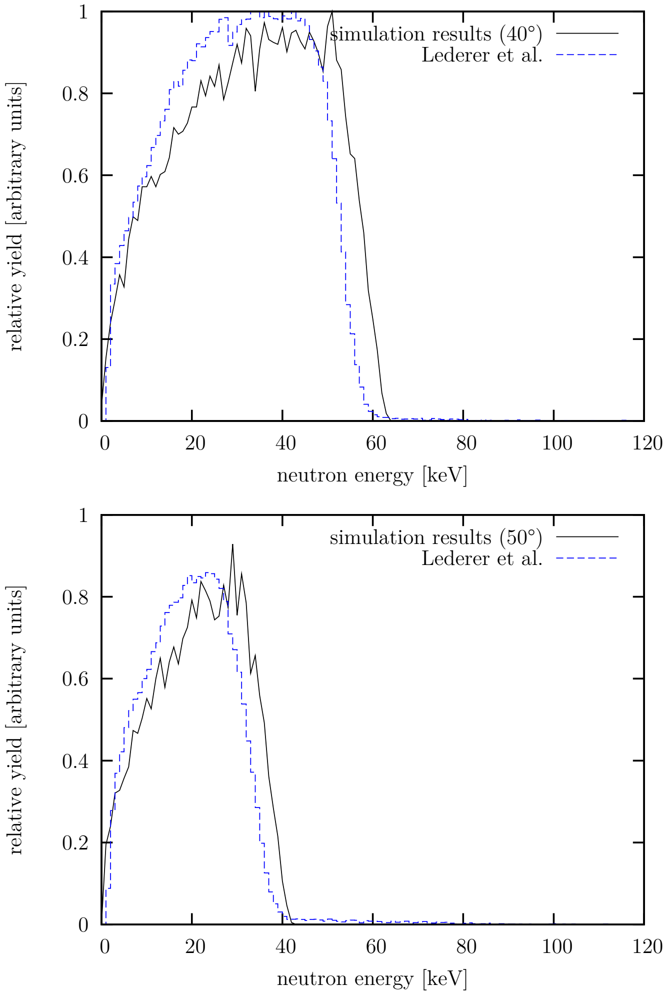

Figure 3.7.: Side-by-side comparison of simulated angular distributions with preliminary results from Physikalisch-Technische Bundesanstalt.

4. Neutron beam properties at FRANZ

With a high quality neutron beam being the main goal of any neutron source, it is important to know the neutron beam properties available for an experiment. For the FRANZ project aiming at high neutron fluxes, the flux available at the sample in question is very important. In time of flight mode, the collimating channel will shield a significant percentage of the beam, allowing only neutrons with emission angles near 0° to actually continue their way to the sample.

Depicted in Figure 4.1 is the neutron flight path in time of flight mode after having been produced in the ^{7}Li target on the left. They pass the collimator of length l_1 and hit the sample in the center of the 4π detector array at $l_1 + d$. Every neutron that does not react passes on until it exists the detector array at $l_1 + 2\,d + l_2$. In order to make sure that no neutron can hit the exit detector module, the diameter of the collimator needs to be chosen appropriately. In this figure, two lines indicate the maximum angle under which a neutron may be emitted (depending on its position) in order *not* to hit the last module. The angle between these two lines can be calculated at the intersection point in the sample:

$$\tan\frac{\alpha}{2} = \frac{d_1/2}{l_1 + d} \qquad \tan\frac{\alpha}{2} = \frac{d_2/2}{l_2 + d} \qquad \tan\frac{\alpha}{2} = \frac{d_3/2}{d}$$

$$\frac{d_1}{l_1 + d} = \frac{d_2}{l_2 + d} \qquad \frac{d_3}{d} = \frac{d_2}{l_2 + d}$$

$$d_1 = \frac{l_1 + d}{l_2 + d}\,d_2 \qquad d_3 = \frac{d}{l_2 + d}\,d_2$$

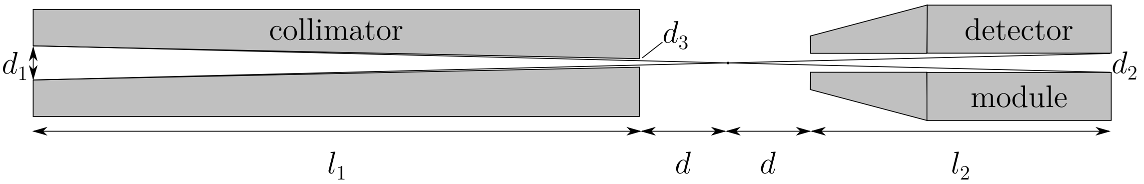

Figure 4.1.: Schematic view of the neutron flight path. The production target is vertically centered at the left with neutrons flying to the right.
Not to scale.

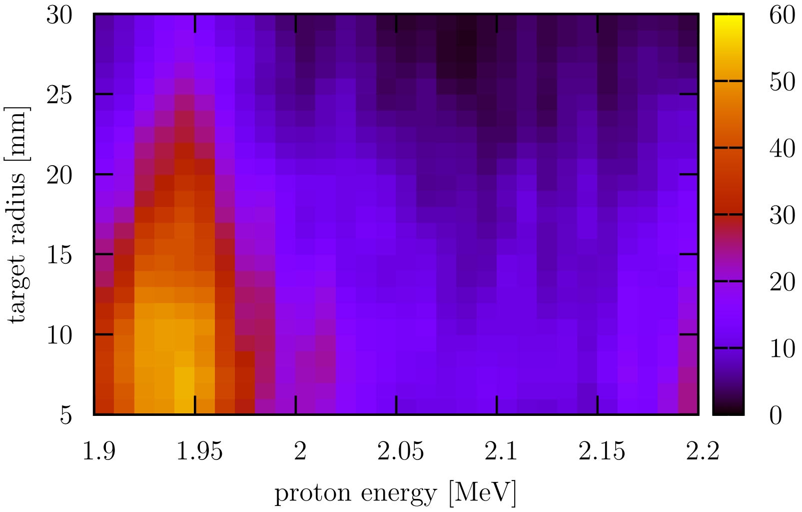

Figure 4.2.: Neutron yield at the sample resulting from an incident parallel proton beam homogeneously distributed over the target's area with the collimator as described in Figure 4.1. The yield increase around 1.95 MeV is connected to the higher zero-degree cross section in this area (see section 3.1).

By employing $l_1 + d = 80\,\text{cm}$ [12, 44], $l_2 + d > 45\,\text{cm}$, $d = 10\,\text{cm}$ [2, p. 602], and $d_2 = 5\,\text{cm}$ [2, p. 604], the required diameters of the collimator are

$$d_1 < 8.89\,\text{cm} \qquad\qquad d_3 < 1.11\,\text{cm}$$

Therefore, the exit hole at the end of the collimator restricts the usable target size: assuming a parallel, homogenous proton beam, Figure 4.2 shows that small target diameters will provide higher neutron counts at the target. Beyond 2 cm, the yield reduces significantly, so the target radius should stay below this threshold. While larger radii relax the situation for beam dynamics – because of space charge forces the particles in a proton pulse are increasingly accelerated outwards when packed tighter – target construction becomes more challenging: The sub-millimeter holes need to be thrilled through a larger volume, thus requiring higher precision. Additionally, the thickness of a few micrometers across the whole target surface needs to be maintained, too, in order not to modify the neutron spectrum (especially by stopping, section 1.3.4). However, current calculations show that the proton beam spot will fit very well on a target with 15 mm radius (cf. Figure 4.3).

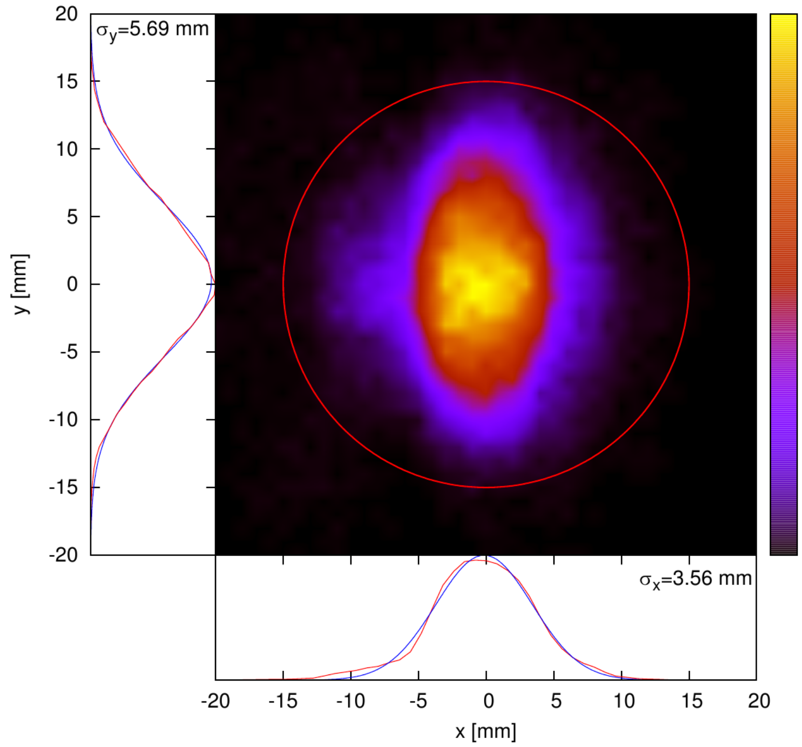

Figure 4.3.: Beam spot on the target for $\Delta E_{\text{rebuncher}} = 0\,\text{keV}$ [45]. The red circle denotes a target of 15 mm radius which is more than twice the standard deviation of the largest σ, namely σ_y.

The phase space projections of such a beam are given on the left side of Figure 4.6 with the resulting neutron distribution on the right side. The center of the proton distribution is at the surface of the target ($z = 300\,\mathrm{mm}$), while the neutron distribution is given after all protons have passed the target. The x–v_x plane reveals the sub-structure of the proton pulse, which consists of nine microbunches merged to a single pulse by the bunch compressor (see section 1.1). At the front of the neutron production target, these microbunches are spatially inseparable. Apparently, this sub-structure does not translate to the neutrons. As can be seen on the right side of Figure 4.6, the neutron beam does not exhibit any similar fragmentation.

The Mollweide plot at the top of Figure 4.6 shows that neutrons are concentrated in a cone with $\theta \approx 70°$ but a significant amount of neutral particles is emitted at $\theta > 70°$. In contrast to Figure 3.2 where all proton energies are below 1.912 MeV, the proton distribution here contains protons with energies reaching up to 2.236 MeV. There, kinematic collimation is not in effect anymore. Similarly, in Figure 4.4 neutrons have already been produced even though the mean proton energy $\langle E_\mathrm{p} \rangle = 1.850\,\mathrm{MeV}$ is below the threshold energy $E_\mathrm{thresh} \approx 1.881\,\mathrm{MeV}$. Again, the input distribution contains particles with more than 2 MeV that produce a small number of neutrons the emission angle of which is not confined by kinematic collimation.

In Figure 4.4–4.8, the rebuncher varies the final proton energy from $\Delta E_\mathrm{rebuncher} \approx -200\,\mathrm{keV}$ to $\Delta E_\mathrm{rebuncher} \approx +200\,\mathrm{keV}$ in steps of 100 keV resulting in different proton distributions. For each step, three phase space projections of the input distribution is given together with the corresponding neutron projections. With increasing $\Delta E_\mathrm{rebuncher}$, the proton beam is accelerated while its spatial extents remain largely unchanged. In contrast, the neutron distribution's x and y dimensions increase from less than 40 mm to approximately 80 mm.

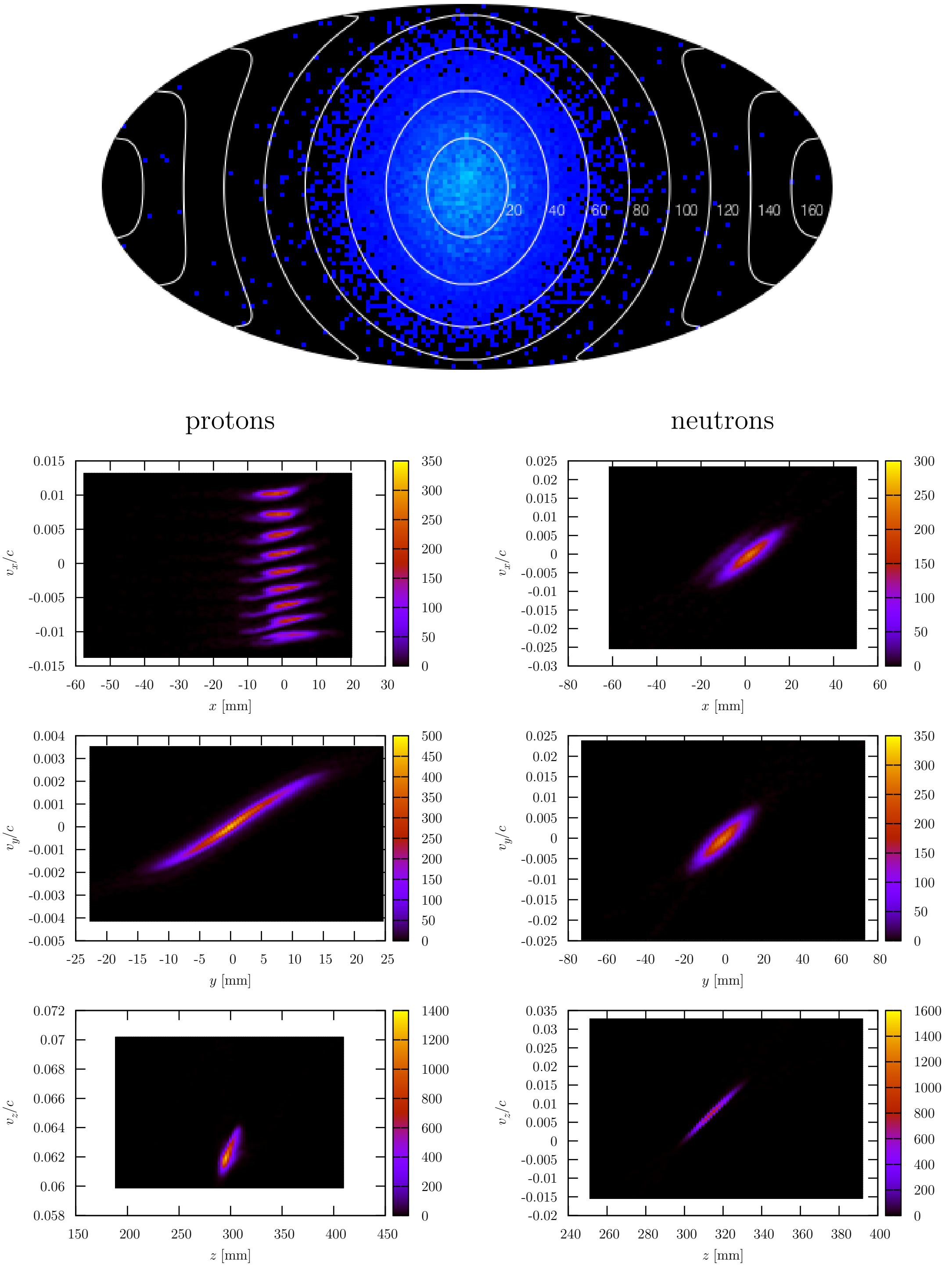

Figure 4.4.: Upper image: Neutron distribution as Mollweide plot. Lower images: Proton and neutron distribution in the x–v_x, y–v_y, and z–v_z planes. With $\Delta E_{\text{rebuncher}} \approx -200\,\text{keV}$, the mean proton energy is $\langle E_\text{p} \rangle = 1.850\,\text{MeV}$.

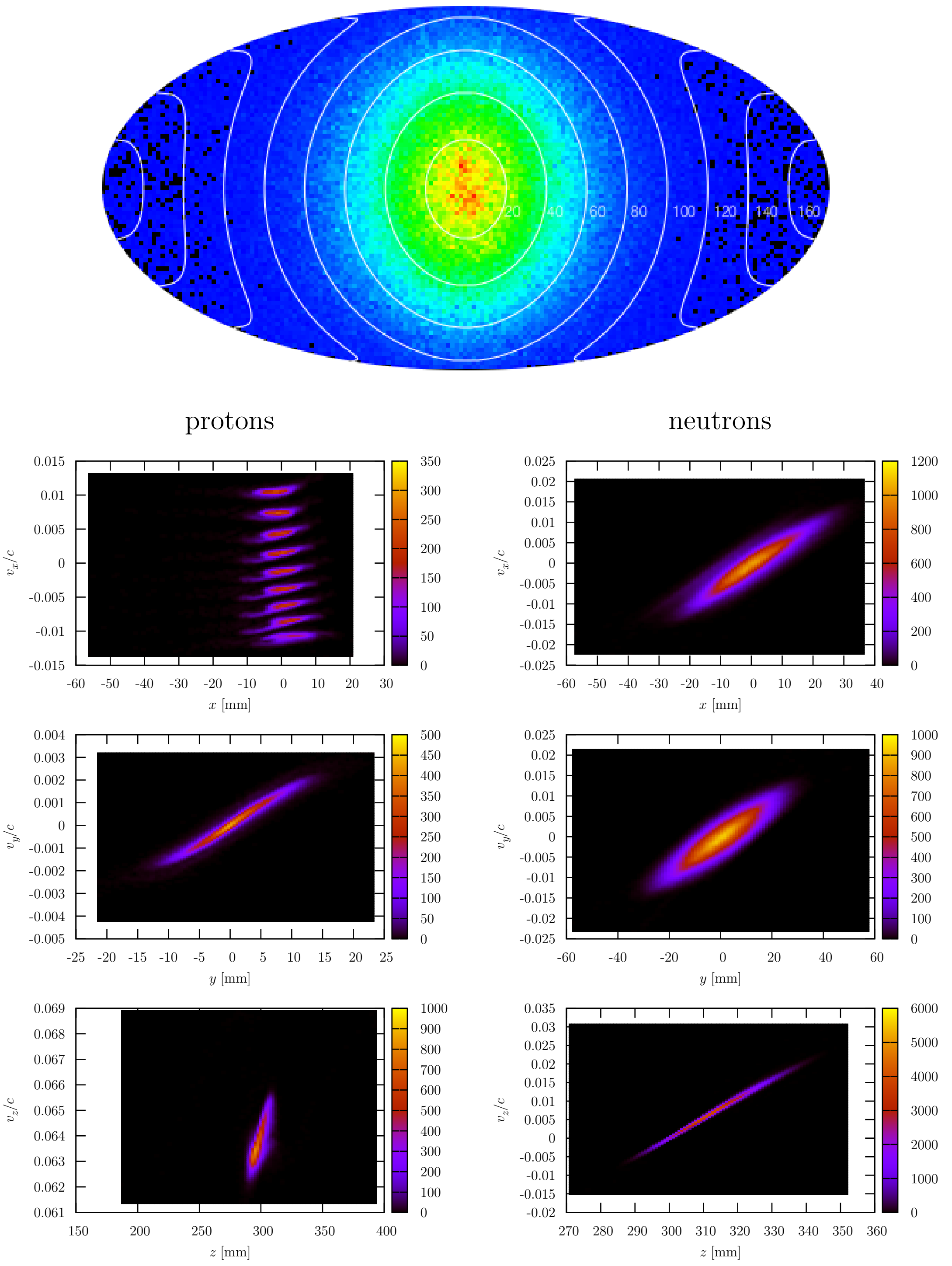

Figure 4.5.: Like Figure 4.4, but with $\Delta E_{\text{rebuncher}} \approx -100\,\text{keV}$ resulting in $\langle E_{\text{p}} \rangle = 1.940\,\text{MeV}$.

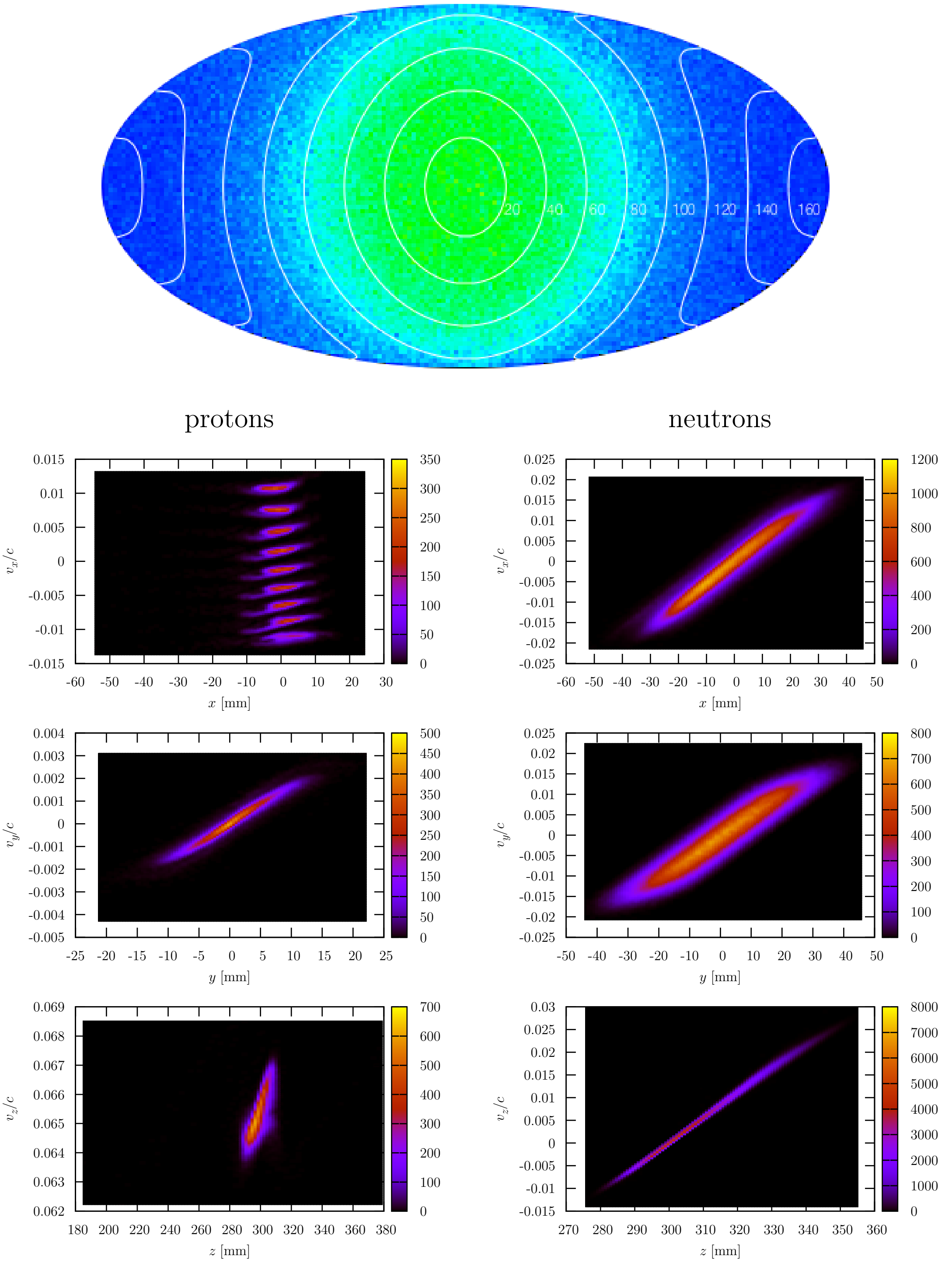

Figure 4.6.: Like Figure 4.4, but with $\Delta E_{\mathrm{rebuncher}} \approx 0\,\mathrm{keV}$ resulting in $\langle E_{\mathrm{p}} \rangle = 2.034\,\mathrm{MeV}$.

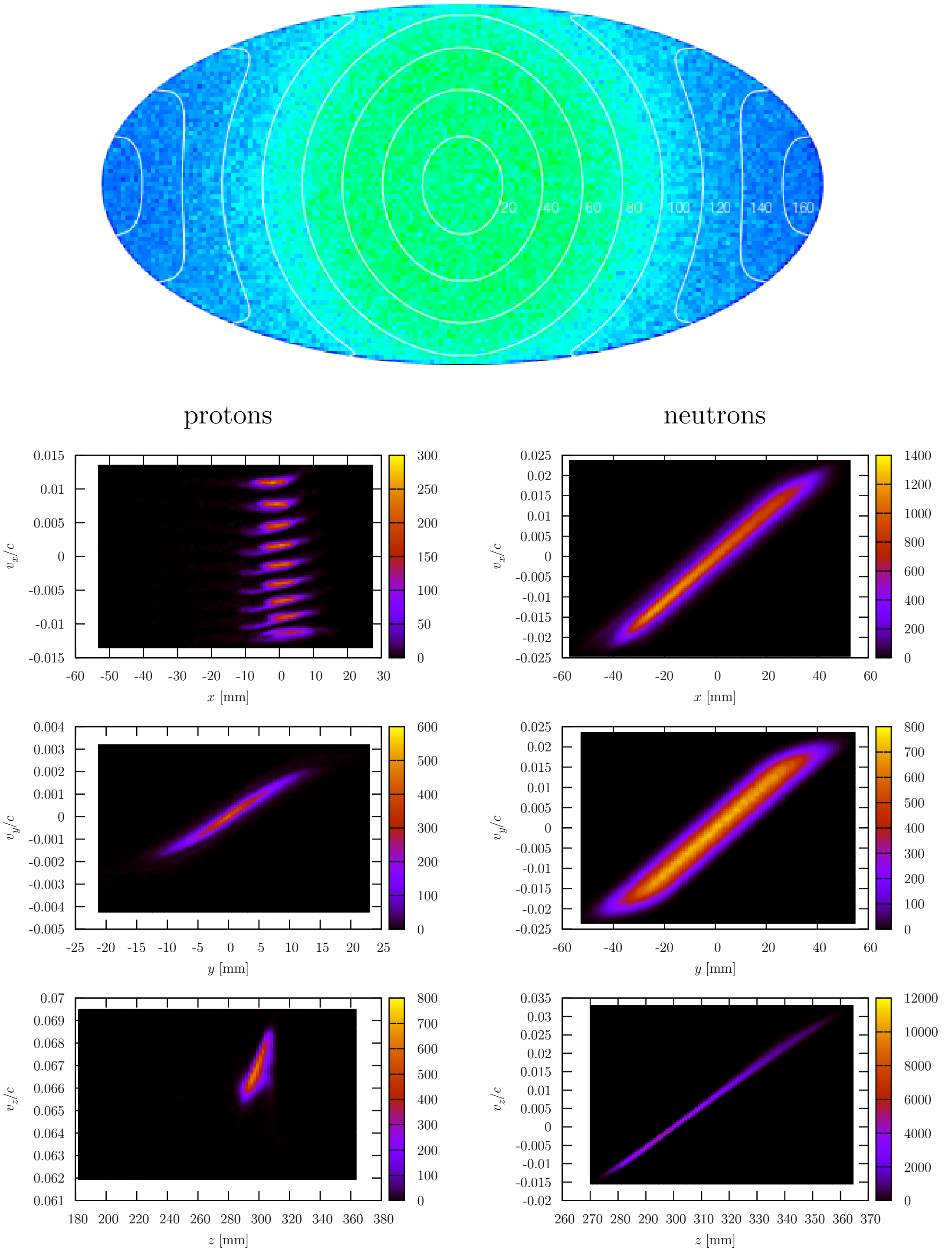

Figure 4.7.: Like Figure 4.4, but with $\Delta E_{\text{rebuncher}} \approx +100\,\text{keV}$ resulting in $\langle E_{\text{p}} \rangle = 2.129\,\text{MeV}$.

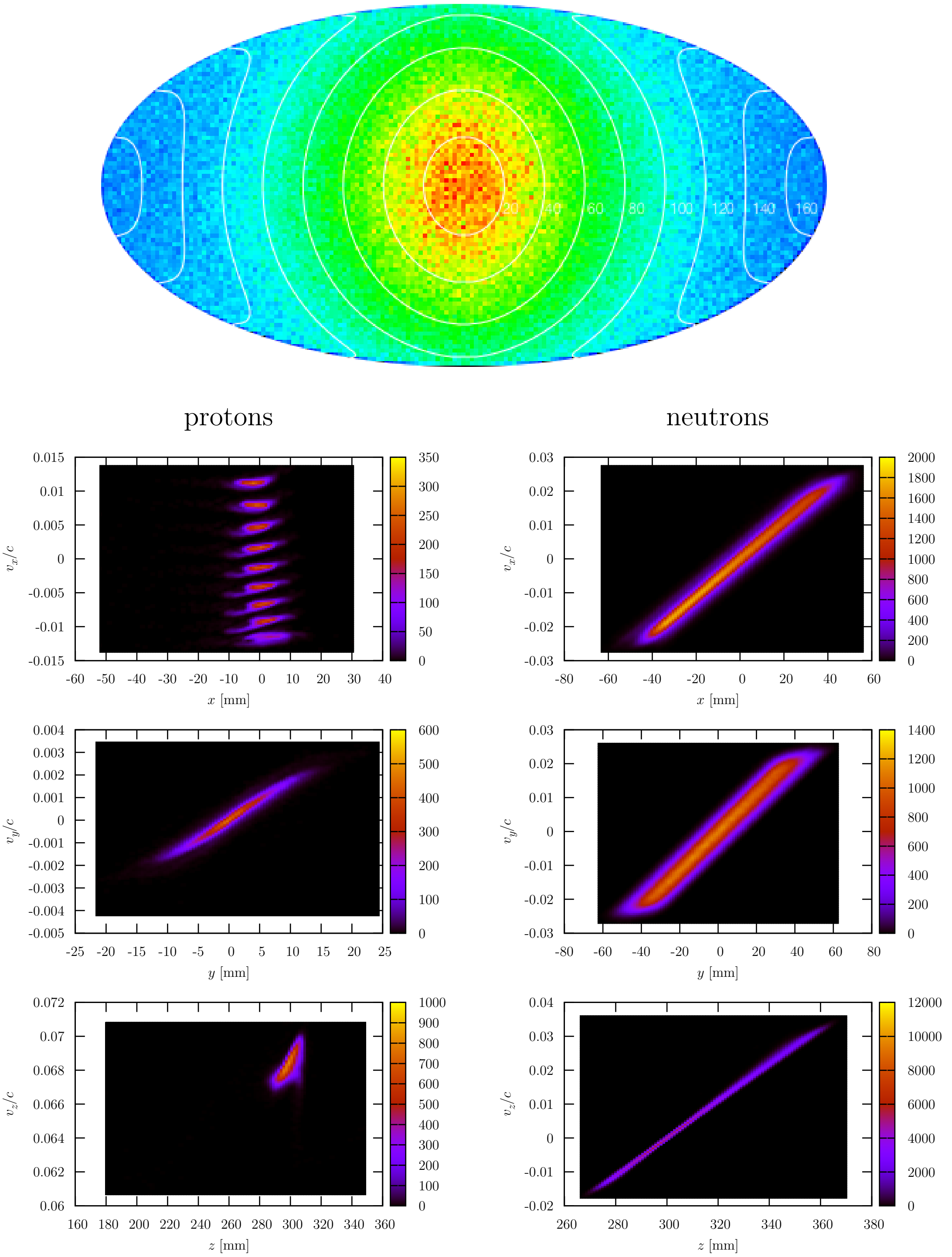

Figure 4.8.: Like Figure 4.4, but with $\Delta E_{\text{rebuncher}} \approx +200\,\text{keV}$ resulting in $\langle E_{\text{p}} \rangle = 2.225\,\text{MeV}$.

5. Conclusion

The program “n17” developed for this thesis has been shown to fulfill the specified requirements very well. It can reproduce experimentally measured neutron spectra even including predictions for the angular distributions as well as the expected neutrons-per-protons ratio. Although the model used in this code may seem simple, it is apparently very capable of reflecting the measurements.

The code was written with FRANZ in mind as one possible application among many others. Working with arbitrary target shapes, the program can be used for target development in both solid and liquid aggregate state, as for example used at the Soreq Applied Research Accelerator Facility in Israel. The produced neutron distribution can be plotted using a Mollweide sphere projection which is intuitively accessible because of its similarity with typical world maps. This can help identify zones of different levels of neutron flux which is important e.g. when designing the radiation protection of a new source. In the context of end-to-end simulations, the program can help optimize the neutron flux according to the experimental requirements as done at FRANZ, for example to increase the flux at the sample. Additionally, predictions of an experiment’s outcome may help interpret its results and hint at whether there may have been systematic problems during its execution. The possibility to compute phase space projections not only provides the possibility to relate the properties of the neutron beam to those of the proton beam but it also enables the characterization of the neutron distribution using well-known terms from proton beam physics.

Beside these currently implemented features, there are many ways to refine the current functionality as well as extend its spectrum of possible applications. Minor updates may implement elastic scattering and procedures to correctly work with space charge aiming at a more complete physical description. Major enhancements should be the inclusion of further possible reaction pathways to improve the predictive capabilities beyond near-threshold energies. It might even be desirable to include further neutron production reactions like ^{9}Be(p, n)^{9}B thereby allowing to study the transfer of proton energies in other reactions. Additional reaction pathways would also be important to enable “n17” to track neutrons in the backing of high-power targets, where water flows in the way of the neutrons. There, n + H reactions should be taken into account because the momentum transfer to hydrogen is maximal. Studying the behaviour of neutrons inside moderators and shieldings using the developed code also requires the inclusion of other reactions. However, shielding design is a very important aspect, as the safe absorption of the the uncharged particles is the basis for safe operation of any neutron source.

Bibliography

[1] Enrico Fermi: *The development of the first chain reacting pile.* Proceedings of the American Philosophical Society, 90(1):20–24, 1946.

[2] K. Wisshak, K. Guber, F. Käppeler, J. Krisch, H. Müller, G. Rupp, and F. Voss: *The Karlsruhe 4π barium fluoride detector.* Nuclear Instruments and Methods in Physics Research A, 292:595–618, July 1990.

[3] Edwin Hubble: *A Relation between Distance and Radial Velocity among Extra-Galactic Nebulae.* Proceedings of the National Academy of Sciences of the United States of America, 15(3):168–173, 1929.

[4] Barry F. Madore, Wendy L. Freedman, N. Silbermann, Paul Harding, John Huchra, Jeremy R. Mould, John A. Graham, Laura Ferrarese, Brad K. Gibson, Mingsheng Han, John G. Hoessel, Shaun M. Hughes, Garth D. Illingworth, Randy Phelps, Shoko Sakai, and Peter Stetson: *A Cepheid distance to the Fornax cluster and the local expansion rate of the Universe.* Nature, 395:47–50, 1998.

[5] Wendy L. Freedman *et al.*: *Final Results from the Hubble Space Telescope Key Project to Measure the Hubble Constant.* The Astrophysical Journal, 553:47–72, 2001.

[6] C. Arlandini, M. Heil, F. Käppeler, R. Reifarth, F. Voss und K. Wisshak: *Sternmodelle im Test: Die Phase der Roten Riesen.* Forschungszentrum-Nachrichten 2/2001, Seiten 177–188.

[7] Edward Anders and Nicolas Grevesse: *Abundances of the elements: Meteoritic and solar.* Geochimica et Cosmochimica Acta, 53(1):197 – 214, 1989.

[8] E. Margaret Burbidge, G. R. Burbidge, William A. Fowler, and F. Hoyle: *Synthesis of the Elements in Stars.* Rev. Mod. Phys., 29(4):547–650, October 1957.

[9] R. Reifarth, R. C. Haight, M. Heil, F. Käppeler, and D. J. Vieira: *Neutron capture measurements at a ria-type facility.* Nuclear Instruments and Methods in Physics Research Section A: Accelerators, Spectrometers, Detectors and Associated Equipment, 524(1–3):215 – 226, 2004.

[10] Stefan Schmidt: *Gamma Measurements with the* 4π *BaF*$_2$ *Detector Array for the FRANZ Facility.* Bachelor's thesis, 2008. `http://publikationen.ub.uni-frankfurt.de/volltexte/2009/6269/`.

[11] Oliver Meusel: *The planned high intensity neutron facility FRANZ.* Workshop on modern methods using fast neutrons for research related to the transmutation of nuclear waste, EFNUDAT collaboration and users meeting, Forschungszentrum Dresden-Rossendorf, February 13–15, 2008.

[12] O. Meusel, L.P. Chau, I. Mueller, U. Ratzinger, A. Schempp, K. Volk, and C. Zhang: *Development of an Intense Neutron Source "FRANZ" in Frankfurt.* Proceedings of LINAC 2006, Knoxville, United States of America.

[13] R. Norenberg, U. Ratzinger, J. Sun, and K. Volk: *Development of a high efficiency proton source for the Frankfurter-Neutronen-Quelle am Stern-Gerlach-Zentrum.* Review of Scientific Instruments, 79(2):02B316, 2008.

[14] Ian G. Brown (editor): *The physics and technology of ion sources.* Wiley-VCH Verlag, second, revised and extended edition, 2004.

[15] Christoph Wiesner: *Schnelles Choppersystem für hochintensive Protonenstrahlen.* Diploma thesis, 2008. `http://publikationen.ub.uni-frankfurt.de/volltexte/2009/6992/`.

[16] C. Wiesner, L. P. Chau, H. Dinter, M. Droba, N. Joshi, O. Meusel, I. Mueller, and U. Ratzinger: *E×B Chopper System for High Intensity Proton Beams.* Proceedings of LINAC 2010, Tsukuba, Japan, September 12–17 2010.

[17] Long Phi Chau, Martin Droba, Ninad Joshi, Oliver Meusel, Ulrich Ratzinger, and Christoph Wiesner: *One Nanosecond Bunch Compressor for Intense Proton Beams.* Proceedings of EPAC 2008, Genoa, Italy.

[18] Long Phi Chau, Martin Droba, Oliver Meusel, Daniel Noll, Ulrich Ratzinger, and Christoph Wiesner: *Bunch Compressor For Intense Proton Beams.* Proceedings of LINAC 2010, Tsukuba, Japan.

[19] D. Petrich, M. Heil, F. Käppeler, J. Kaltenbaek, E. P. Knaetsch, K. Litfin, D. Roller, W. Seith, R. Stieglitz, F. Voss, and S. Walter: *A neutron production target for FRANZ.* Nuclear Instruments and Methods in Physics Research Section A: Accelerators, Spectrometers, Detectors and Associated Equipment, 596(3):269–275, 2008.

[20] René Reifarth: *The s-process – overview and selected recent developments.* Nuclear Physics in Astrophysics IV, Frascati, Italy, June 2009.

[21] R. R. Kinsey *et al.*: *The NUDAT/PCNUDAT Program for Nuclear Data.* Paper submitted to the 9th International Symposium of Capture-Gamma ray Spectroscopy and Related Topics, October 1996.

[22] M. Drosg: *Monoenergetic neutron production by two-body reactions in the energy range from 0.0001 to 500 MeV. An overview*, October 1999. `http://homepage.univie.ac.at/Manfred.Drosg/drosg99.pdf`, visited on Sept. 29, 2010.

[23] Horst Liskien and Arno Paulsen: *Neutron production cross sections and energies for the reactions* $^{7}Li(p,n)^{7}Be$ *and* $^{7}Li(p,n)^{7}Be^{*}$. Atomic Data and Nuclear Data Tables, 15(1):57–84, 1975.

[24] V. S. Siksin, V. N. Domoratsky, L. V. Donetskov, A. N. Voronin, M. M. Novikov, A. N. Kudryavtsev, G. D. Batyshchev, S. K. Barvin, and V. F. Tseshkovskaya: *Differential cross sections of proton elastic scattering on Be nuclei and the total cross section of reaction* $^{9}Be(p,n)^{9}B$ *near the treshold.* Atomnaya Energiya, 12:15, 1970.

[25] L.G. Earwaker, J.G. Jenkin, and E.W. Titterton: *The* $^{10}B(p,n)^{10}C$ *excitation function from threshold to 10.6 MeV.* Nuclear Physics, 42:521 – 528, 1963.

[26] K. Ramavataram, R. Larue, V. Turcotte, C. St. Pierre, and S. Ramavataram: *Study of the* $^{11}B(p,n)^{11}C$ *reaction below the giant dipole resonance in* ^{12}C *near the treshold.* Nuovo Cimento A, 58:342, 1980.

[27] C. H. Johnson, C. C. Trail, and A. Galonsky: *Thresholds for (p, n) Reactions on 26 Intermediate-Weight Nuclei.* Phys. Rev., 136(6B):B1719–B1729, December 1964.

[28] Bogdan Povh, Klaus Rith, Christoph Scholz und Frank Zetsche: *Teilchen und Kerne.* Springer, 7. Auflage, 2006.

[29] F. Ajzenberg-Selove: *Energy levels of light nuclei* $A = 5$*–10.* Nuclear Physics A, 490(1):1–225, 1988.

[30] Wolfgang Demtröder: *Experimentalphysik 4 – Kern-, Teilchen- und Astrophysik.* Springer, 2. Auflage, 2005.

[31] R. E. White, P. H. Barker, and D. M. J. Lovelock: *Measurement of Nuclear Reaction Q-values with High Accuracy:* $^{7}Li(p,n)^{7}Be$. Metrologia, 21(4):193, 1985.

[32] G. Audi, A. H. Wapstra, and C. Thibault: *The AME2003 atomic mass evaluation: (II). Tables, graphs and references.* Nuclear Physics A, 729(1):337–676, 2003. The 2003 NUBASE and Atomic Mass Evaluations.

[33] James Ziegler: *Handbook of Stopping Cross-Sections for Energetic Ions in all Elements*, volume 5. Pergamon Press, New York, 1980.

[34] Daniel Noll: *Strahldynamikoptimierung und Rebuncher für den FRANZ Bunchkompressor.* HICforFAIR Workshop „Aktuelle Probleme der Beschleuniger- und Plasmaphysik“, Riezlern, Österreich, 7.–13. März 2010.

[35] G. Feinberg, M. Paul, A. Arenshtam, D. Berkovits, D. Kijel, A. Nagler, and I. Silverman: *LiLiT – a Liquid-Lithium Target as an Intense Neutron Source for Nuclear Astrophysics at the Soreq Applied Research Accelerator Facility.* Nuclear Physics A, 827(1-4):590c–592c, 2009. PANIC08 – Proceedings of the 18th Particles and Nuclei International Conference.

[36] Patrick Reichart: *Relativistische Kinematik – Formelsammlung*, Dezember 1996. `http://www.e12.physik.tu-muenchen.de/stud/vorlesungen/misc/relkin.pdf`, besucht: 23. September 2010.

[37] John P. Snyder: *Map Projections: A Working Manual.* U.S. Geological Survey Professional Paper 1395, Washington, DC: U.S. Government Printing Office, 1987.

[38] D. Petrich, F. Käppeler, L. Kazakov und O. Meusel: *Auslegung und Simulation der Abschirmung von FRANZ.*

[39] René Reifarth, Michael Heil, Franz Käppeler, and Ralf Plag: *PINO—a tool for simulating neutron spectra resulting from the* ^{7}*Li(p,n) reaction.* Nuclear Instruments and Methods in Physics Research A, 608(1):139–143, 2009.

[40] W. Ratynski and F. Käppeler: *Neutron capture cross section of* ^{197}*Au: A standard for stellar nucleosynthesis.* Phys. Rev. C, 37(2):595–604, February 1988.

[41] W. Ratynski and F. Käppeler: *Neutron capture cross section of* ^{197}*Au: A standard for stellar nucleosynthesis.* Phys. Rev. C, 37(2):595–604, February 1988. Private communication F. Käppeler.

[42] A.D. Carlson, V.G. Pronyaev, D.L. Smith, N.M. Larson, Zhenpeng Chen, G.M. Hale, F. J. Hambsch, E.V. Gai, Soo Youl Oh, S.A. Badikov, T. Kawano, H.M. Hofmann, H. Vonach, and S. Tagesen: *International Evaluation of Neutron Cross Section Standards.* Nuclear Data Sheets, 110(12):3215 – 3324, 2009. Special Issue on Nuclear Reaction Data.

[43] Claudia Lederer, Iris Dillmann, Ulrich Giesen, Franz Käppeler, Alberto Mengoni, Marita Mosconi, Ralf Nolte, and Anton Wallner: *Definition of a standard neutron field with the reaction* ^{7}*Li(p, n)*^{7}*Be.* Unpublished.

[44] U. Ratzinger, L. P. Chau, H. Dinter, M. Droba, M. Heilmann, N. Joshi, D. Mäder, A. Metz, O. Meusel, I. Müller, Y. Nie, D. Noll, H. Podlech, R. Reifarth, H. Reichau, A. Schempp, S. Schmidt, W. Schweizer, K. Volk, C. Wagner, and C. Wiesner: *The Frankfurt Neutron Source FRANZ.* The 1st International Particle Accelerator Conference, Kyoto, Japan, May 23–28th, 2010.

[45] Daniel Noll. Private communications.

[46] *ICRU-Report 49: Stopping Powers and Ranges for Protons and Alpha Particles.* 1993.

[47] H. Vogel: *Gerthsen Physik*, Band 20. Springer-Verlag, 1980.

A. Energy interchange

For both the classical and relativistic description of the energy interchange in the ^{7}Li(p, n)^{7}Be reaction, the ^{7}Li nucleus is assumed at rest while the incident proton completely carries the kinetic energy of the system. In order to retain a concise notation, in this section all kinetic energies are referred to as T, while total energies are denoted by $E = T + mc^2$.

The assumptions can be summarized as

$$v_{\mathrm{Li}} = 0 \qquad T_{\mathrm{Li}} = \frac{1}{2} m_{\mathrm{Li}} v_{\mathrm{Li}}^2 = 0 \tag{A.1a}$$

$$v_{\mathrm{p}} \neq 0 \qquad T_{\mathrm{p}} = \frac{1}{2} m_{\mathrm{p}} v_{\mathrm{p}}^2 \neq 0 \tag{A.1b}$$

$$Q = (m_{\mathrm{Li}} + m_{\mathrm{p}} - m_{\mathrm{Be}} - m_{\mathrm{n}})c^2 \tag{A.1c}$$

A.1. Classical description

In the classical description, the center of mass transformation eases the calculation because there

$$p_{\mathrm{tot}}^{\mathrm{CM}} = 0$$

is valid resulting in

$$p_{\mathrm{Li}}^{\mathrm{CM}} + p_{\mathrm{p}}^{\mathrm{CM}} = 0 = p_{\mathrm{Be}}^{\mathrm{CM}} + p_{\mathrm{n}}^{\mathrm{CM}} \tag{A.2}$$

while in the lab system only

$$\underbrace{p_{\mathrm{Li}}}_{\overset{\text{(A.1a)}}{=} 0} + p_{\mathrm{p}} = p_{\mathrm{Be}} + p_{\mathrm{n}} \tag{A.3}$$

holds. The center of mass can be considered as a particle with mass m_{CM} and velocity v_{CM} defined by

$$m_{\mathrm{CM}} = \sum_i m_i$$
$$v_{\mathrm{CM}} = \frac{\sum_i m_i v_i}{\sum_i m_i}$$

However, as the classical description does not properly account for masses converting into kinetic energy, the center of mass properties between initial state (index "i") and final state (index "f") differ if the particles' masses change.

$$m_{\mathrm{CM,i}} = m_{\mathrm{Li}} + m_{\mathrm{p}} \qquad v_{\mathrm{CM,i}} = \frac{m_{\mathrm{Li}} v_{\mathrm{Li}} + m_{\mathrm{p}} v_{\mathrm{p}}}{m_{\mathrm{Li}} + m_{\mathrm{p}}} \overset{\text{(A.1a)}}{=} \frac{m_{\mathrm{p}}}{m_{\mathrm{Li}} + m_{\mathrm{p}}} v_{\mathrm{p}} \tag{A.4}$$

$$m_{\mathrm{CM,f}} = m_{\mathrm{Be}} + m_{\mathrm{n}} \qquad v_{\mathrm{CM,f}} = \frac{m_{\mathrm{Be}} v_{\mathrm{Be}} + m_{\mathrm{n}} v_{\mathrm{n}}}{m_{\mathrm{Be}} + m_{\mathrm{n}}} \tag{A.5}$$

So it is possible that $m_{\mathrm{CM,i}} \neq m_{\mathrm{CM,f}}$. The possible discrepancy to (A.4) becomes visible when combining (A.3) and (A.5).

$$\begin{aligned} m_{\mathrm{p}} v_{\mathrm{p}} &= m_{\mathrm{Be}} v_{\mathrm{Be}} + m_{\mathrm{n}} v_{\mathrm{n}} \\ &\overset{\text{(A.5)}}{=} \left(m_{\mathrm{Be}} + m_{\mathrm{n}}\right) v_{\mathrm{CM,f}} \\ v_{\mathrm{CM,f}} &= \frac{m_{\mathrm{p}}}{m_{\mathrm{Be}} + m_{\mathrm{n}}} v_{\mathrm{p}} \end{aligned}$$

With (A.4), the center of mass' initial kinetic energy $T_{\mathrm{CM,i}}$ in the lab system can be calculated using

$$\begin{aligned} T_{\mathrm{CM,i}} &= \frac{1}{2} m_{\mathrm{CM,i}} v_{\mathrm{CM,i}}^2 \\ &\overset{\text{(A.4)}}{=} \frac{1}{2} (m_{\mathrm{Li}} + m_{\mathrm{p}}) \left(\frac{m_{\mathrm{p}}}{m_{\mathrm{Li}} + m_{\mathrm{p}}} v_{\mathrm{p}} \right)^2 \\ &= \frac{1}{2} \frac{m_{\mathrm{p}}^2}{m_{\mathrm{Li}} + m_{\mathrm{p}}} v_{\mathrm{p}}^2 \\ &= \frac{m_{\mathrm{p}}}{m_{\mathrm{Li}} + m_{\mathrm{p}}} T_{\mathrm{p}} \end{aligned}$$

So in the center of mass system, the available kinetic energy prior to the interaction is given by

$$\begin{aligned} T_{\mathrm{i}}^{\mathrm{CM}} &= T_{\mathrm{Li}} + T_{\mathrm{p}} - T_{\mathrm{CM,i}} \\ &\overset{\text{(A.1a)}}{=} T_{\mathrm{p}} - T_{\mathrm{CM,i}} \\ &= T_{\mathrm{p}} - \frac{m_{\mathrm{p}}}{m_{\mathrm{Li}} + m_{\mathrm{p}}} T_{\mathrm{p}} \\ &= \frac{m_{\mathrm{Li}}}{m_{\mathrm{Li}} + m_{\mathrm{p}}} T_{\mathrm{p}} \end{aligned} \tag{A.6}$$

while after the interaction it is

$$T_{\mathrm{f}}^{\mathrm{CM}} = T_{\mathrm{i}}^{\mathrm{CM}} + Q \tag{A.7}$$

Because of energy conservation, the latter energy must be distributed among the neutron and the ^{7}Be nucleus according to

$$T_\mathrm{f}^\mathrm{CM} = \frac{1}{2} m_\mathrm{Be} \left(v_\mathrm{Be}^\mathrm{CM}\right)^2 + \frac{1}{2} m_\mathrm{n} \left(v_\mathrm{n}^\mathrm{CM}\right)^2 \tag{A.8}$$

where the relation between $v_\mathrm{Be}^\mathrm{CM}$ and v_n^CM is determined by (A.2), i.e.

$$\begin{aligned} 0 &= m_\mathrm{Be} v_\mathrm{Be}^\mathrm{CM} + m_\mathrm{n} v_\mathrm{n}^\mathrm{CM} \\ v_\mathrm{Be}^\mathrm{CM} &= -\frac{m_\mathrm{n}}{m_\mathrm{Be}} v_\mathrm{n}^\mathrm{CM} \end{aligned} \tag{A.9}$$

By inserting (A.9) into (A.8), the energy of the neutron in the center of mass system T_n^CM can be derived

$$\begin{aligned} T_\mathrm{f}^\mathrm{CM} &= \frac{1}{2} m_\mathrm{Be} \left(-\frac{m_\mathrm{n}}{m_\mathrm{Be}} v_\mathrm{n}^\mathrm{CM}\right)^2 + \frac{1}{2} m_\mathrm{n} \left(v_\mathrm{n}^\mathrm{CM}\right)^2 \\ &= \frac{m_\mathrm{n}}{m_\mathrm{Be}} T_\mathrm{n}^\mathrm{CM} + T_\mathrm{n}^\mathrm{CM} \\ T_\mathrm{n}^\mathrm{CM} &= \frac{m_\mathrm{Be}}{m_\mathrm{Be} + m_\mathrm{n}} T_\mathrm{f}^\mathrm{CM} \end{aligned}$$

resulting in

$$v_\mathrm{n}^\mathrm{CM} = \sqrt{\frac{2\, T_\mathrm{n}^\mathrm{CM}}{m_\mathrm{n}}} \qquad \text{and} \qquad p_\mathrm{n}^\mathrm{CM} = \sqrt{2\, T_\mathrm{n}^\mathrm{CM}\, m_\mathrm{n}} \tag{A.10}$$

To transform this result back to the lab system, the velocity of the center of mass after the interaction, $v_\mathrm{CM,f}$, is required. Combining (A.3) with (A.5) yields

$$\begin{aligned} m_\mathrm{p} v_\mathrm{p} &= m_\mathrm{Be} v_\mathrm{Be} + m_\mathrm{n} v_\mathrm{n} \\ &= (m_\mathrm{Be} + m_\mathrm{n}) v_\mathrm{CM,f} \\ v_\mathrm{CM,f} &= \frac{m_\mathrm{p}}{m_\mathrm{Be} + m_\mathrm{n}} v_\mathrm{p} \end{aligned}$$

Therefore, the neutron velocity in the lab system is

$$\begin{aligned} v_\mathrm{n} &= v_\mathrm{n}^\mathrm{CM} + v_\mathrm{CM,f} \qquad (A.11) \\ &= \sqrt{\frac{2\, T_\mathrm{n}^\mathrm{CM}}{m_\mathrm{n}}} + \frac{m_\mathrm{p}}{m_\mathrm{Be} + m_\mathrm{n}} v_\mathrm{p} \end{aligned}$$

A.2. Relativistic description

The more general relativistic discussion in [36] can be simplified because of the initial assumptions given in (A.1). These translate into the four momenta

$$P_{\mathrm{Li}} = \begin{pmatrix} m_{\mathrm{Li}} c \\ 0 \end{pmatrix} \qquad\qquad P_{\mathrm{p}} = \begin{pmatrix} T_{\mathrm{p}}/c + m_{\mathrm{p}} c \\ p_{\mathrm{p}} \end{pmatrix}$$

where p_{p} can be calculated using the relativistic energy-momentum equation

$$\begin{aligned} E_{\mathrm{p}}^2 &= p_{\mathrm{p}}^2 c^2 + m_{\mathrm{p}}^2 c^4 = \left(T_{\mathrm{p}} + m_{\mathrm{p}} c^2\right)^2 \\ p_{\mathrm{p}} &= \frac{1}{c}\sqrt{\left(T_{\mathrm{p}} + m_{\mathrm{p}} c^2\right)^2 - m_{\mathrm{p}}^2 c^4} \\ &= \frac{1}{c}\sqrt{T_{\mathrm{p}}^2 + 2\,T_{\mathrm{p}}\, m_{\mathrm{p}} c^2} \end{aligned} \tag{A.12}$$

The invariant total energy of the center of mass is given by

$$\begin{aligned} E_{\mathrm{CM}}^2 &= \left(P_{\mathrm{Li}} + P_{\mathrm{p}}\right)^2 c^2 \\ &= \left(m_{\mathrm{Li}} c^2 + T_{\mathrm{p}} + m_{\mathrm{p}} c^2\right)^2 - \left(0 + p_{\mathrm{p}} c\right)^2 \\ &\overset{(A.12)}{=} m_{\mathrm{Li}}^2 c^4 + T_{\mathrm{p}}^2 + m_{\mathrm{p}}^2 c^4 \\ &\qquad + 2\,T_{\mathrm{p}}\, m_{\mathrm{Li}} c^2 + 2\, m_{\mathrm{Li}} c^2\, m_{\mathrm{p}}^2 c^4 + 2\,T_{\mathrm{p}}\, m_{\mathrm{p}} c^2 \\ &\qquad - T_{\mathrm{p}}^2 - 2\,T_{\mathrm{p}}\, m_{\mathrm{p}} c^2 \\ &= m_{\mathrm{Li}}^2 c^4 + m_{\mathrm{p}}^2 c^4 + 2\,T_{\mathrm{p}}\, m_{\mathrm{Li}} c^2 + 2\, m_{\mathrm{Li}} c^2\, m_{\mathrm{p}}^2 c^4 \\ &= \left(m_{\mathrm{Li}} c^2 + m_{\mathrm{p}} c^2\right)^2 + 2\,T_{\mathrm{p}}\, m_{\mathrm{Li}} c^2 \\ E_{\mathrm{CM}} &= \sqrt{\left(m_{\mathrm{Li}} c^2 + m_{\mathrm{p}} c^2\right)^2 + 2\,T_{\mathrm{p}}\, m_{\mathrm{Li}} c^2} \\ &= \left(m_{\mathrm{Li}} c^2 + m_{\mathrm{p}} c^2\right)\sqrt{1 + \frac{2\,T_{\mathrm{p}}\, m_{\mathrm{Li}} c^2}{\left(m_{\mathrm{Li}} c^2 + m_{\mathrm{p}} c^2\right)^2}} \end{aligned}$$

from which the kinetic energy available in the center of mass system can be derived using

$$\begin{aligned} T_{\mathrm{i}}^{\mathrm{CM}} &= E_{\mathrm{CM}} - \left(m_{\mathrm{Li}} c^2 + m_{\mathrm{p}} c^2\right) \\ &= \left(m_{\mathrm{Li}} c^2 + m_{\mathrm{p}} c^2\right)\left[\sqrt{1 + \frac{2\,T_{\mathrm{p}}\, m_{\mathrm{Li}} c^2}{\left(m_{\mathrm{Li}} c^2 + m_{\mathrm{p}} c^2\right)^2}} - 1\right] \end{aligned} \tag{A.13}$$

This is the relativistic equivalent of (A.6) – if the rest mass is much larger than the kinetic energy, i.e. $\frac{2\,T_{\mathrm{p}}\, m_{\mathrm{Li}} c^2}{\left(m_{\mathrm{Li}} c^2 + m_{\mathrm{p}} c^2\right)^2} \ll 1$, the classical solution can be obtained by applying the Taylor approximation $\sqrt{1+x} \approx 1 + \frac{1}{2}x$ (for $x \ll 1$) to (A.13).

As in the classical description, the Q value relates the initial kinetic energy in the center of mass to its final value, so (A.7) also holds in the relativistic case. However, its explicit use is not required since the mass difference between input and output channel are accounted for because of the consideration of total energies instead of plain kinetic energies. To finally detemine the neutron's speed, using the momentum conservation described by (A.2) is required. Employing the energy-momentum equation gives

$$\begin{aligned}
\left(p_{\mathrm{Be}}^{\mathrm{CM}}\right)^2 &= \left(p_{\mathrm{n}}^{\mathrm{CM}}\right)^2 \\
\left(E_{\mathrm{Be}}^{\mathrm{CM}}\right)^2 - m_{\mathrm{Be}}^2 c^4 &= \left(E_{\mathrm{n}}^{\mathrm{CM}}\right)^2 - m_{\mathrm{n}}^2 c^4 \\
\left(E_{\mathrm{Be}}^{\mathrm{CM}}\right)^2 - \left(E_{\mathrm{n}}^{\mathrm{CM}}\right)^2 &= m_{\mathrm{Be}}^2 c^4 - m_{\mathrm{n}}^2 c^4 \\
\underbrace{\left(E_{\mathrm{Be}}^{\mathrm{CM}} + E_{\mathrm{n}}^{\mathrm{CM}}\right)}_{E_{\mathrm{CM}}} \left(E_{\mathrm{Be}}^{\mathrm{CM}} - E_{\mathrm{n}}^{\mathrm{CM}}\right) &= m_{\mathrm{Be}}^2 c^4 - m_{\mathrm{n}}^2 c^4 \\
E_{\mathrm{Be}}^{\mathrm{CM}} - E_{\mathrm{n}}^{\mathrm{CM}} &= \frac{m_{\mathrm{Be}}^2 c^4 - m_{\mathrm{n}}^2 c^4}{E_{\mathrm{CM}}} \qquad \text{(A.14)}
\end{aligned}$$

By replacing $E_{\mathrm{Be}}^{\mathrm{CM}} = E_{\mathrm{CM}} - E_{\mathrm{n}}^{\mathrm{CM}}$, the neutron's total energy in the center of mass system can be deduced:

$$\begin{aligned}
E_{\mathrm{CM}} - 2\,E_{\mathrm{n}}^{\mathrm{CM}} &= \frac{m_{\mathrm{Be}}^2 c^4 - m_{\mathrm{n}}^2 c^4}{E_{\mathrm{CM}}} \\
E_{\mathrm{n}}^{\mathrm{CM}} &= \frac{E_{\mathrm{CM}}}{2} - \frac{m_{\mathrm{Be}}^2 c^4 - m_{\mathrm{n}}^2 c^4}{2\,E_{\mathrm{CM}}} \\
p_{\mathrm{n}}^{\mathrm{CM}} &= \frac{1}{c}\sqrt{\left(E_{\mathrm{n}}^{\mathrm{CM}}\right)^2 - m_{\mathrm{n}}^2 c^4} \qquad \text{from } E^2 = p^2c^2 + m^2c^4
\end{aligned}$$

Again, in the classical limit of $m_{\mathrm{n}}c^2 \gg T_{\mathrm{n}}$, $p_{\mathrm{n}}^{\mathrm{CM}}$ is equivalent to the classical value (A.10), which can be analyzed by replacing $E_{\mathrm{n}}^{\mathrm{CM}}$ and factoring out $m_{\mathrm{n}}c^2$:

$$\begin{aligned}
p_{\mathrm{n}}^{\mathrm{CM}} &= \frac{1}{c}\sqrt{\left(T_{\mathrm{n}}^{\mathrm{CM}} + m_{\mathrm{n}}c^2\right)^2 - m_{\mathrm{n}}^2 c^4} \\
&= \frac{1}{c}\sqrt{2\,T_{\mathrm{n}}^{\mathrm{CM}}\, m_{\mathrm{n}}c^2 + \left(T_{\mathrm{n}}^{\mathrm{CM}}\right)^2} \\
&= \frac{1}{c} m_{\mathrm{n}}c^2 \sqrt{\frac{2\,T_{\mathrm{n}}^{\mathrm{CM}}}{m_{\mathrm{n}}c^2} + \underbrace{\left(\frac{T_{\mathrm{n}}^{\mathrm{CM}}}{m_{\mathrm{n}}c^2}\right)^2}_{\approx 0}} \\
&= \sqrt{2\,T_{\mathrm{n}}^{\mathrm{CM}}\, m_{\mathrm{n}}c^2}
\end{aligned}$$

and with $v = \beta\, c = \frac{p\,c}{E} c$, the classical neutron velocity can be obtained (compare (A.10)):

$$\begin{aligned}
v_\mathrm{n}^\mathrm{CM} &= \frac{p_\mathrm{n}^\mathrm{CM}\, c}{E_\mathrm{n}^\mathrm{CM}} c = c\, \frac{\sqrt{\left(E_\mathrm{n}^\mathrm{CM}\right)^2 - m_\mathrm{n}^2 c^4}}{E_\mathrm{n}^\mathrm{CM}} \\
&= c\, \frac{\sqrt{\left(m_\mathrm{n} c^2 + T_\mathrm{n}^\mathrm{CM}\right)^2 - m_\mathrm{n}^2 c^4}}{m_\mathrm{n} c^2 + T_\mathrm{n}^\mathrm{CM}} \\
&= c\, \frac{\sqrt{\left(1 + \frac{2\,T_\mathrm{n}^\mathrm{CM}}{m_\mathrm{n} c^2} + \left(\frac{T_\mathrm{n}^\mathrm{CM}}{m_\mathrm{n} c^2}\right)^2\right) - 1}}{1 + \frac{T_\mathrm{n}^\mathrm{CM}}{m_\mathrm{n} c^2}} \\
&= c\, \frac{\sqrt{\frac{2\,T_\mathrm{n}^\mathrm{CM}}{m_\mathrm{n} c^2} + \overbrace{\left(\frac{T_\mathrm{n}^\mathrm{CM}}{m_\mathrm{n} c^2}\right)^2}^{\approx 0}}}{\underbrace{1 + \frac{T_\mathrm{n}^\mathrm{CM}}{m_\mathrm{n} c^2}}_{\approx 1}} \\
&\approx \sqrt{\frac{2\,T_\mathrm{n}^\mathrm{CM}}{m_\mathrm{n}}}
\end{aligned}$$

To transform p_n^CM and E_n^CM back to the lab frame, an inverse Lorentz transformation is required. Note that in contrast to the classical description, the center of mass velocity required for this transformation does not change during the reaction as can be seen when applying momentum conservation (A.3) and energy conservation ($E_\mathrm{Li} + E_\mathrm{p} = E_\mathrm{Be} + E_\mathrm{n}$):

$$\beta_\mathrm{CM} := \beta_\mathrm{CM,i} = \frac{p_\mathrm{Li} + p_\mathrm{p}}{E_\mathrm{Li} + E_\mathrm{p}} c = \frac{p_\mathrm{Be} + p_\mathrm{n}}{E_\mathrm{Be} + E_\mathrm{n}} c = \beta_\mathrm{CM,f}$$

which in the classical limit yields (compare (A.4))

$$v_\mathrm{CM} = \beta_\mathrm{CM} c = c\, \frac{p_\mathrm{p}\, c}{m_\mathrm{Li} c^2 + E_\mathrm{p}} \approx c\, \frac{p_\mathrm{p} c}{m_\mathrm{Li} c^2 + m_\mathrm{p} c^2} = \frac{m_\mathrm{p}}{m_\mathrm{Li} + m_\mathrm{p}} v_\mathrm{p}$$

Therefore, the Lorentz boost with $\beta = -\beta_\mathrm{CM}$ is given by

$$\begin{aligned}
\begin{pmatrix} E_\mathrm{n}/c \\ p_\mathrm{n} \end{pmatrix} &= \gamma_\mathrm{CM} \begin{pmatrix} 1 & +\beta_\mathrm{CM} \\ +\beta_\mathrm{CM} & 1 \end{pmatrix} \begin{pmatrix} E_\mathrm{n}^\mathrm{CM}/c \\ p_\mathrm{n}^\mathrm{CM} \end{pmatrix} \\
&= \gamma_\mathrm{CM} \begin{pmatrix} E_\mathrm{n}^\mathrm{CM}/c + \beta_\mathrm{CM}\, p_\mathrm{n}^\mathrm{CM} \\ \beta_\mathrm{CM}\, E_\mathrm{n}^\mathrm{CM}/c + p_\mathrm{n}^\mathrm{CM} \end{pmatrix}
\end{aligned}$$

Finally, the neutron velocity can be expressed as

$$\begin{aligned}
v_{\mathrm{n}} &= \beta_{\mathrm{n}} c \\
&= c\,\frac{p_{\mathrm{n}} c}{E_{\mathrm{n}}} \\
&= c\,\frac{\beta_{\mathrm{CM}}\,E_{\mathrm{n}}^{\mathrm{CM}} + p_{\mathrm{n}}^{\mathrm{CM}} c}{E_{\mathrm{n}}^{\mathrm{CM}} + \beta_{\mathrm{CM}}\,p_{\mathrm{n}}^{\mathrm{CM}} c} && \Big|\ \times\frac{1/E_{\mathrm{n}}^{\mathrm{CM}}}{1/E_{\mathrm{n}}^{\mathrm{CM}}} \\
&= c\,\frac{\beta_{\mathrm{CM}} + \beta_{\mathrm{n}}^{\mathrm{CM}}}{1 + \beta_{\mathrm{CM}}\,\beta_{\mathrm{n}}^{\mathrm{CM}}} \\
&= \frac{v_{\mathrm{CM}} + v_{\mathrm{n}}^{\mathrm{CM}}}{1 + \frac{v_{\mathrm{CM}}\,v_{\mathrm{n}}^{\mathrm{CM}}}{c^2}} \qquad \text{(A.15)}
\end{aligned}$$

which is the addition formula for the velocity classically given by $v_{\mathrm{CM}} + v_{\mathrm{n}}^{\mathrm{CM}}$.

B. Stopping power

In Figure B.1, the incident nucleus with charge Q passes through the target losing energy through momentum transfer. The transversal momentum transfer is given by

$$\Delta p = \int\limits_{-\infty}^{+\infty} F \,\mathrm{d}t = \frac{1}{v}\int\limits_{-\infty}^{+\infty} F \,\mathrm{d}x = \frac{1}{v}\int\limits_{-\infty}^{+\infty} qE_\perp \,\mathrm{d}x = \frac{q}{v}\int\limits_{-\infty}^{+\infty} E_\perp \,\mathrm{d}x \tag{B.1}$$

where $E_\perp$ stands for the electric field orthogonal to $\vec{v}$. The integral $\int_{-\infty}^{+\infty} E_\perp \,\mathrm{d}x$ can be derived from Maxwell's equations

$$\begin{aligned} \vec{\nabla}\vec{E} &= \frac{\rho}{\epsilon_0} \\ \int \vec{\nabla}\vec{E}\,\mathrm{d}V &= \int \frac{\rho}{\epsilon_0}\,\mathrm{d}V \\ \oint \vec{E}\,\mathrm{d}\vec{A} &= \int \frac{\rho}{\epsilon_0}\,\mathrm{d}V \end{aligned} \tag{B.2}$$

Since inside the cylinder (cf. Figure B.1) the only charge is Q, the right side of (B.2) can easily be evaluated. For the left side, $E_\perp$ is always perpendicular to the cylinder barrel resulting in

$$\oint \vec{E}\,\mathrm{d}\vec{A} = \int E_\perp\, 2\pi b \,\mathrm{d}x \qquad \text{and} \qquad \int \frac{\rho}{\epsilon_0}\,\mathrm{d}V = \frac{Q}{\epsilon_0}$$

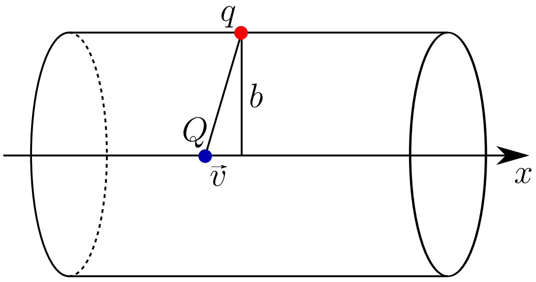

Figure B.1.: Illustration for the derivation of the energy loss. Q stands for a stopped nucleus, while q denotes an electron inside the stopping material. The impact parameter is given by b.

$$\int E_\perp \, \mathrm{d}x = \frac{1}{4\pi\epsilon_0} \frac{2\,Q}{b} \tag{B.3}$$

Together with (B.1), the energy transfer to the electron ΔE yields

$$\begin{aligned} \Delta E &= \frac{(\Delta p)^2}{2\,m_\mathrm{e}} \\ &= \left(\frac{1}{4\pi\epsilon_0}\right)^2 \frac{2\,q^2\,Q^2}{m_\mathrm{e} v^2\, b^2} \end{aligned}$$

In order to calculate the total energy per path section dx transferred from the incident particle, $-\frac{\mathrm{d}E}{\mathrm{d}x}$, the electron density n_e multiplied by the energy loss per electron ΔE has to be integrated over the circular area A orthogonal to the x axis.

$$-\frac{\mathrm{d}E}{\mathrm{d}x} = \int\limits_A n_\mathrm{e}\,\Delta E \; \mathrm{d}A$$

or in cylindrical coordinates

$$\begin{aligned} -\frac{\mathrm{d}E}{\mathrm{d}x} &= \int\limits_{b_\mathrm{min}}^{b_\mathrm{max}} \int\limits_0^{2\pi} n_\mathrm{e}\,\Delta E\, b \; \mathrm{d}\varphi \; \mathrm{d}b \\ &= 2\pi \int\limits_{b_\mathrm{min}}^{b_\mathrm{max}} n_\mathrm{e}\,\Delta E\, b \; \mathrm{d}b \\ &= \left(\frac{1}{4\pi\epsilon_0}\right)^2 \frac{4\pi\, q^2\, Q^2\, n_\mathrm{e}}{m_\mathrm{e} v^2} \int\limits_{b_\mathrm{min}}^{b_\mathrm{max}} \frac{1}{b} \; \mathrm{d}b \\ &= \left(\frac{1}{4\pi\epsilon_0}\right)^2 \frac{4\pi\, q^2\, Q^2\, n_\mathrm{e}}{m_\mathrm{e} v^2} \ln \frac{b_\mathrm{max}}{b_\mathrm{min}} \end{aligned} \tag{B.4}$$

Since the electrons are bound, their excitation energy is not continuous. Instead, there is a minimum energy the electrons can absorb, which corresponds to a maximum impact parameter b_max because the Coulomb energy reduces with increasing distance. b_max is given by the ionization potential I [46]:

$$\begin{aligned} \Delta E_\mathrm{min} &= \left(\frac{1}{4\pi\epsilon_0}\right)^2 \frac{2\,q^2\,Q^2}{m_\mathrm{e} v^2\, b_\mathrm{max}^2} = I \\ b_\mathrm{max} &= \frac{1}{4\pi\epsilon_0} \frac{qQ}{v} \sqrt{\frac{2}{m_\mathrm{e}\, I}} \end{aligned} \tag{B.5}$$

The minimum impact parameter b_{min} is determined by the maximum momentum transfer $(\Delta p)_{\mathrm{max}} = 2\, m_{\mathrm{e}} v$ [47, p. 33].

$$\begin{aligned} 2\, m_{\mathrm{e}} v = (\Delta p)_{\mathrm{max}} &\overset{(\mathrm{B.1})(\mathrm{B.3})}{=} \frac{1}{4\pi\epsilon_0} \frac{2\, qQ}{v\, b_{\mathrm{min}}} \\ b_{\mathrm{min}} &= \frac{1}{4\pi\epsilon_0} \frac{qQ}{m_{\mathrm{e}} v^2} \end{aligned} \tag{B.6}$$

Inserting (B.5) and (B.6) into (B.4) yields the final result

$$-\frac{\mathrm{d}E}{\mathrm{d}x} = \left(\frac{1}{4\pi\epsilon_0}\right)^2 \frac{4\pi\, q^2\, Q^2\, n_{\mathrm{e}}}{m_{\mathrm{e}} v^2} \ln \sqrt{\frac{2\, m_{\mathrm{e}} v^2}{I}} \tag{B.7}$$

This equation corresponds to the classical Bohr image although it already includes the ionization potential introduced by Bloch. Enhanced by additional corrections for relativistic velocities and effects from quantum mechanics, the formula attributed to Hans Bethe, is [28, p. 366]

$$-\frac{\mathrm{d}E}{\mathrm{d}x} = \left(\frac{1}{4\pi\epsilon_0}\right)^2 \frac{4\pi\, q^2\, Q^2\, n_{\mathrm{e}}}{m_{\mathrm{e}} c^2\, \beta^2} \left[\ln \left(\frac{2\, m_{\mathrm{e}} c^2\, \gamma^2 \beta^2}{I} \right) - \beta^2 \right]$$